GEWEX water vapor assessment (G-VAP)

Report on
“An analysis of the diurnal sampling bias using GNSS data”

Heidrun Höschen, Marc Schröder
DWD, Offenbach, Germany

Issue/Revision Index: **1.0**

Date: **30.08.2016**

Document Change Record

Issue/ Revision	Date	Change record (author)
1.0	30/08/2016	Final version, H. Höschen, M. Schröder

Table of Contents

Purpose

This report summarises the results of the activity “An analysis of the diurnal sampling bias using GNSS data” which was dedicated to support the GEWEX water vapor assessment (G-VAP). The report is part of the Appendix of the G-VAP final report, and an executive summary has been included in the main part of the final report.

1 Introduction

Atmospheric water vapour content plays a key role in the atmospheric water cycle and is influencing the Earth’s radiation budget and the atmospheric chemistry. The Global Climate Observing System (GCOS) and the World Climate Research Programme (WCRP) demand for a coordinated international assessment of climate products, among others water vapour. The aim of the World Climate Research Programme Global Energy and Water Cycle Experiment (GEWEX) is among others to observe, understand and model the hydrological cycle in the Earth's atmosphere (www.gewex.org). The GEWEX Data and Assessments Panel (GDAP) founded the water vapour assessment (GVAP, www.gewex-vap.org) to select reasonable water vapour products for climate application. Stable time series of water vapour measurements are needed for model applications as well as for the validation itself. Inconsistencies need to be found and explained. GVAP focuses on the investigations of stability of all three GCOS Essential Climate Variables (ECV), i.e. precipitable water, upper tropospheric humidity and water vapour and related temperature profiles.

In 1992 the idea of using the GPS signal delay to calculate the atmospheric water vapour content came up (Bevis et al., 1992), was proven to work with sub-mm accuracy (Rocken et al., 1993) and to agree with radiometer measurements to 1-2 mm RMS (Rocken et al., 1995). GPS/GNSS measurements were also used to validate data from different satellite measurements like the Moderate Resolution Imaging Spectro-radiometer (MODIS) (Ningombam et al., 2016) or Radiosoundings (Yu et al., 2015), or to investigate the climatology of precipitable water (Jin and Luo, 2009; Bordi et al., 2015).

Polar orbiting satellites overpass a location on the Earth twice daily. In case climatological averages are computed the reduced temporal sampling can lead to systematic (regional) biases if a pronounced diurnal cycle is present. The majority of investigations of the diurnal cycle were focusing on limited areas like Sumatra Island (Wu et al., 2003), Spain (Ortiz et al., 2011), continental United States (Radhakrishna et al., 2015) or South-Central Canada (Hanesiak et al., 2010) and are not combining measurements from different times. A study combining twice-daily synoptic soundings at 0000 and 1200 UTC for radiosounding launches (Dai et al., 2002) over North America found the diurnal sampling error to be within ±3%, while Wang and Zhang (2008) found the diurnal sampling errors of twice-daily radiosonde data to be within 2% in a similar study.

The aim of this study now is to use the extended GNSS database to phenomenologically describe the climatological diurnal cycle, to describe and investigate the associated sampling bias of simulated twice-daily-passing satellites individually as well as combined overpasses at several overflight times and its significance. Also, valuable feedback to GNSS PIs and GNSS users is provided by documenting seeming issues of a few individual stations.

Prior to the presentation of results in sections 4.1-4.3 (diurnal cycle) and sections 4.4-4.5 (bias and standard deviation) the data base, the pre-processing and the methodology is described.

2 Data

This evaluation is based on a 2-hourly data set measured by ground-based Global Positioning System (GPS). Since the atmospheric delay of the signal sent by the satellites and received by the ground stations is dependent on pressure, temperature and total amount of water vapour, the latter can be calculated by knowing pressure and temperature. Those were gained from synoptic observations as well as from the reanalysis of the National Center for Atmospheric Research (NCEP/NCAR). The exact methodology of how precipitable water is derived from the measured zenith path delay is described in detail in Wang et al. (2007). They also found the accuracy of precipitable water is roughly 4 mm.

The GNSS data base version 721.1 includes data from 1995 to 2011. In total, 997 stations are specified, which however not cover the full period. Every station is characterized by latitude, longitude and altitude and provides 2-hourly data that contain day and time (UTC), surface pressure (hPa), atmospheric weighted-mean temperature (K), precipitable water (mm) as well as information about zenith delay. Here we consider precipitable water.

The amount of data per year varies over time and per station. We first identify the 5 year period with maximum data density and define a threshold of 75%. Thus, each period of at least five continuous years was checked regarding how many stations fulfil this requirement. The period from 2004 until 2008 was identified with 179 stations and a complete table can be found in the appendix (Table 1).

A minor issue was found: each December 31st contains no data later than 17 UTC. However, the influence of this issue on this investigation is negligible.

3 Methods

First, the time needs to be converted from UTC to local time (LST). Using the longitude, the local time can easily be calculated via

$$LST = UTC + \frac{12*longitude}{180°}. \qquad (1)$$

The local times are binned into blocks of 2 hours and within each 2 hour bin the values are averaged. With those bins, a satellite that passes twice a day can be simulated by again averaging any bin and the related bin 12 hours later. A threshold of at least 75% of all possible data must be available.

The climatology C is calculated as the mean of all measurements of the years 2004-2008.

Diurnal cycles and total climatology are plotted for each station and month. Examples are presented in sections 4.2.1 and 4.3.1, peculiar stations are presented in section 4.2.3 and in the appendix (Table 2).

The following analysis considers bias, standard deviation, significance tests in absolute and relative units and correlation. The bias is defined here as

$$Bias(x) = \frac{\sum_{i=1}^{n}(x-C)}{n}, \qquad (2)$$

with x the investigated parameter (precipitable water, simulated by averaging bin values at LST and LST+12 hours), C the climatology and n the number of bins that are taken into account.

The standard deviation is then calculated using

$$STD = \sqrt{\frac{\sum_{i=1}^{n} \quad (x-C)^2}{n}}. \qquad (3)$$

The significance is calculated with python's implemented Shapiro-Wilk-test, where the confidence level was set to 95%.

Another part of this evaluation is based on relative variables. Relative is defined here as:

$$Relative\ bias = \frac{Bias}{Mean}. \qquad (4)$$

The time-amplitude-factor is defined as:

$$Time - amplitude - factor = (1 - \frac{LSTdiff}{12})(\frac{Amplitude}{max(Amplitude)}). \qquad (5)$$

with LSTdiff being the absolute smallest time difference between the minimum and the maximum of the diurnal cycle

The correlations of scatterplots are calculated using python's Pearson correlation coefficient.

4 Results

In this section an overview of the diurnal cycle of precipitable water is given first. Then, the bias and the standard deviation are presented and discussed on global scale. A series of potential reasons for the observed biases are also analysed.

In case of seasonal investigations, the classification of the seasons was done with respect to the seasons on the northern hemisphere: Winter therefore includes December, January and February, spring is composed of March, April and May, summer consists of June, July and August while fall is made up of September, October and November.

Generally results related to the virtual overflight time of 4-6 and 16-18 LST are presented. Results for other overflight times are shown in the appendix (see, e.g., Figures 22 and 26).

4.1 Time series

Figure 1 gives the time series of the mean precipitable water over the investigated period. As expected, winter season shows lowest values in precipitable water while summer season has largest values.

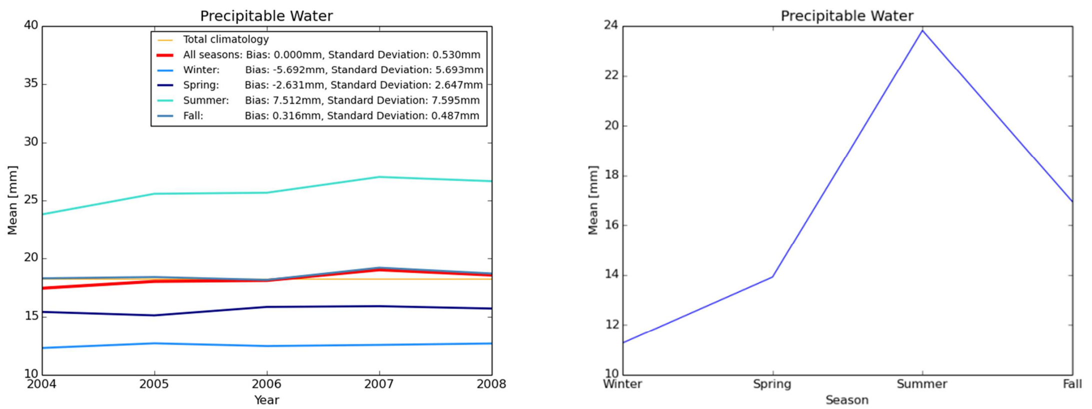

Figure 1. Time series of precipitable water for the period 2004-2008 (left) and annual cycle (right).

4.2 Diurnal Cycles

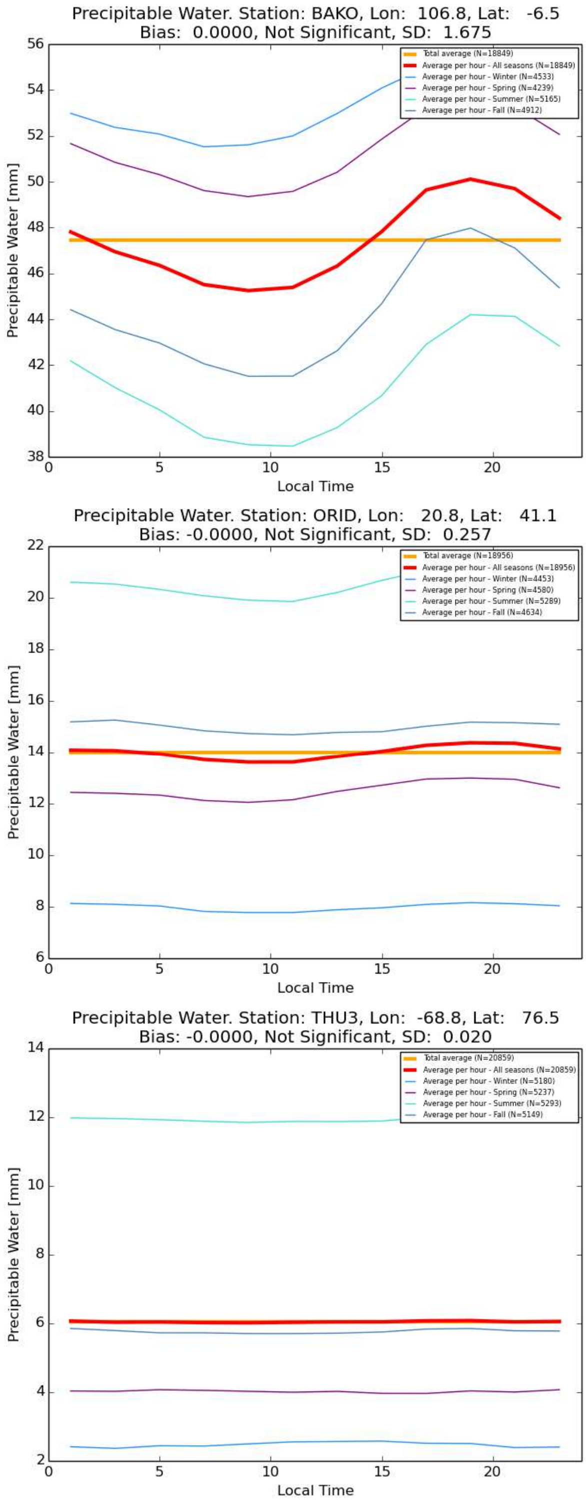

The most distinct diurnal cycle is presented by the Indonesian station *BAKO* (Figure 2), located about 10 miles south of Jakarta and close to the equator with about 6.5° S latitude. A feature of the diurnal cycle is the compressed sinusoidal shape. While the minimum is at about 9 LST the maximum is 10 hours later at about 19 LST. This results in an asymmetric and non-sinusoidal shape of the diurnal cycle. The mean value is about 47 mm and the amplitude is ~5 mm.

Figure 2 also demonstrates the diurnal cycle of precipitable water at station *ORID* in Macedonia at 41.1°N. Here, the mean precipitable water is about 14.3 mm and thus much smaller than the mean at *BAKO*. Since the amplitude has also decreased to about 0.8 instead of 5, this diurnal cycle is more flat (ratios of 0.11 to 0.06). The minimum of precipitable water is at about 11 LST while the maximum is still at about 19 LST, with therefore only 8 hours in between and thus a stronger asymmetry. The diurnal cycle of THU3 has an amplitude of 0.13 mm with a mean of about 6.06 mm (ratio: 0.02 and thus the least pronounced diurnal cycle of the presented examples).

The relative diurnal cycles are presented in the Appendix, section 8.3.

Figure 2. Diurnal cycles of station *BAKO* (top), *ORID* (middle) and *THU3* (bottom).

The seasonal influence is obvious, demonstrated as colored diurnal cycles in figure 2. Since station *BAKO* is on the southern hemisphere, the lowest values can be found in summer, while the northern hemisphere stations *ORID* and *THU3* reveal their lowest values in winter.

The titles of figure 2 gives information about the bias and standard deviation of the diurnal cycle. As expected, the bias is zero. The standard deviation however decreases with latitude and therefore with mean and amplitude.

4.2.1 Probability Density Functions

Here we show the probability density function (PDF) of precipitable water for the stations *BAKO*, *ORID*, and *THU3*.
The southernmost station BAKO, again having its summer in northern hemisphere's winter, has values generally larger than 30 mm during all seasons. During the hottest season this lower level increases even up to 45 mm. The peak and the width of the PDF change with season.
ORID shows a clear seasonal cycle and a broader DPF in spring.
THU3 (Figure 3), close to the Pituffik Airport in western Greenland has a latitude of 76.5° N and hence is the northernmost station with adequate measurement continuity. The PDF of this northernmost station has precipitable water values lower than 20 mm.
All climatologies exhibit a bimodal PDF.

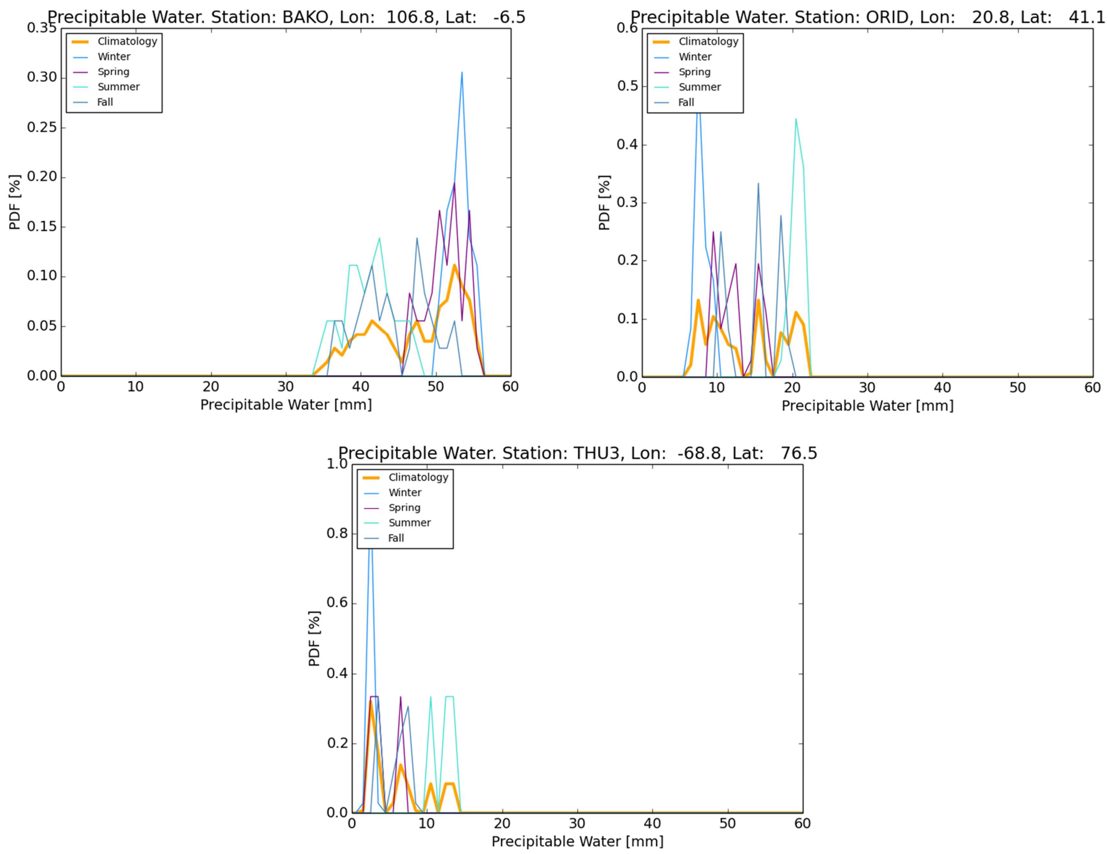

Figure 3. Probability density function of BAKO (upper left), ORID (upper right) and THU3 (bottom).

4.2.2 Peculiar stations

A few stations were found as unusual. As example, station *CAS1* (Figure 3) will be discussed in the following while a complete list of peculiar stations is given in the appendix (see Section 8.2).

Station *CAS1* (Figure 4), located in southern polar regions, exhibits an unusual diurnal cycle. The number of measurements is about equally divided for all times, this influence can therefore be neglected. More interesting is the diurnal cycle of the surface pressure which is clearly anticorrelated to the diurnal cycle of precipitable. The source for pressure is auxiliary data from e.g. synoptic observations (Wang et al., 2007). It should however be mentioned, that the auxiliary data of temperature shows the expected diurnal cycle.

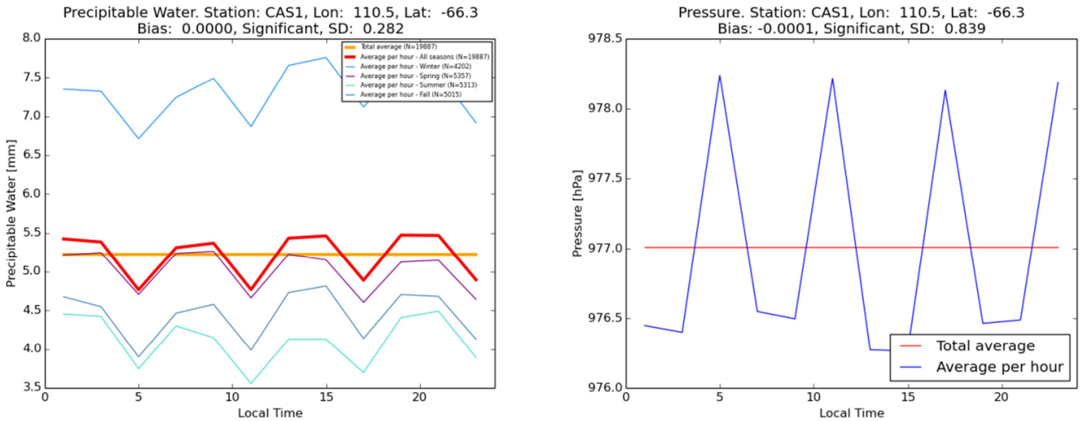

Figure 4. Peculiar station CAS1 in Antarctica. Precipitable water (left) and pressure (right).

An overview of all peculiar stations is given in Appendix 8.2. In total 15 stations are found to be peculiar and such stations are not considered in further analysis.

4.3 Climatology

The mean of precipitable water is largest close to the equator and becomes lower with increasing latitude (Figure 5). While stations whose latitude is higher than 33° usually have mean values lower than 20 mm, maximum values in the tropics are larger than 50 mm. The southern polar regions exhibit less precipitable water than northern polar regions. Maritime stations typically show larger means than continental stations on the same latitude which is to some extend caused by the generally larger elevation of stations on land.

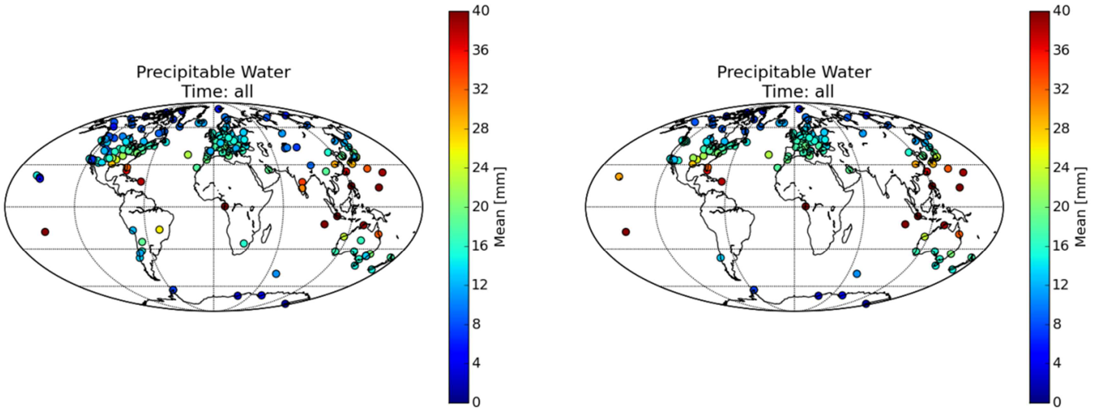

Figure 5. Mean value of precipitable water of all stations (left) and stations with altitudes lower than 500 meters (right).

E.g., two of the four Hawaiian stations *MAUI* (4.1 mm) and *MKEA* (3.6 mm) have vey small values due to their larger elevation (>3000 meters). The obvious dependence on elevation is evident when plotting only stations lower than 500 meters (Figure 5).

4.3.1 Seasonal

Seasonal means (Figure 6) reveal a distinct annual cycle in mid- and higher latitudes by showing largest values in summer on northern hemisphere and vice versa, whereas equatorial stations stay about equal (~55 mm).
The Hawaiian stations *MAUI* and *MKEA* do not follow the annual cycle, they are actually showing a contrary behavior. This is probably linked to their exceptionally large altitude.

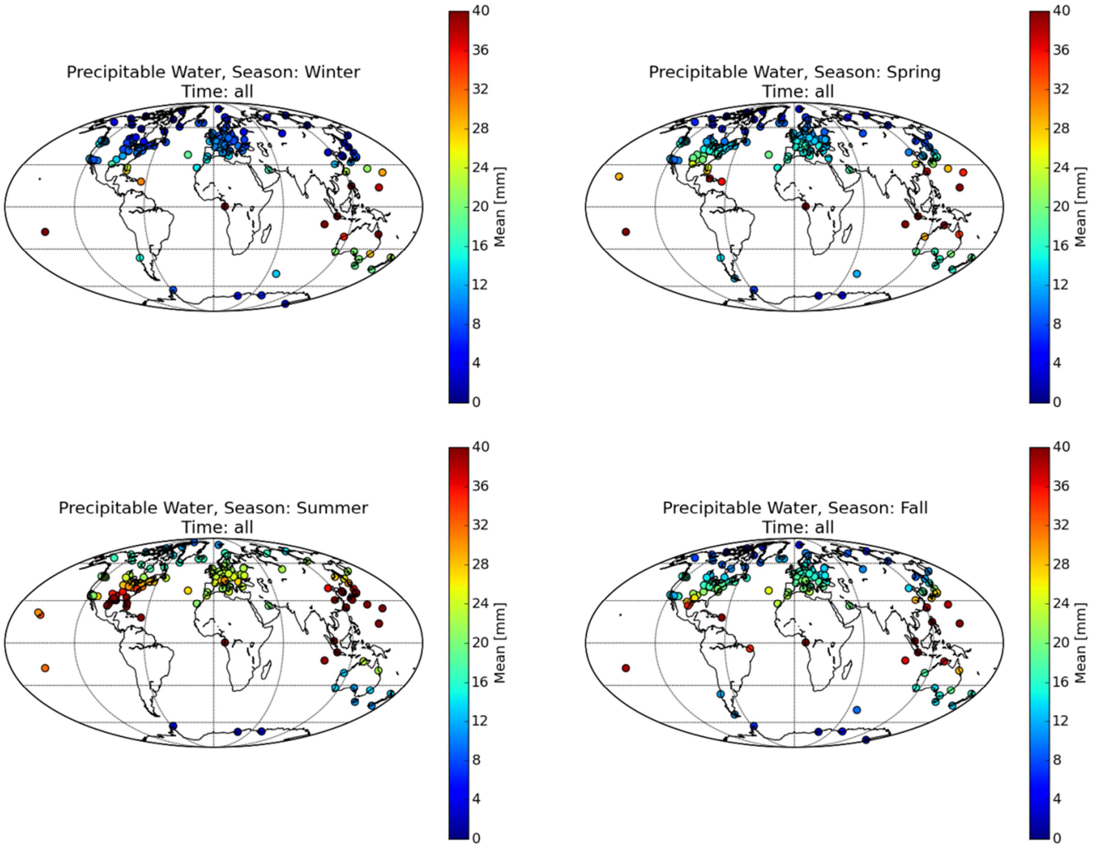

Figure 6. Mean values of precipitable water for several month and seasons. Winter is represented by January (upper left), Spring by April (upper right), Summer by July (lower left) and Fall by October (lower right).

4.3.2 Amplitude and maximum deviation

The amplitude as well as the maximum deviation of the diurnal cycle from the total mean is an indicator for the variability and the flatness of the diurnal cycle. Obviously the amplitude is highly correlated to the maximum deviation, however for a better classification both are illustrated and shortly discussed in this section.

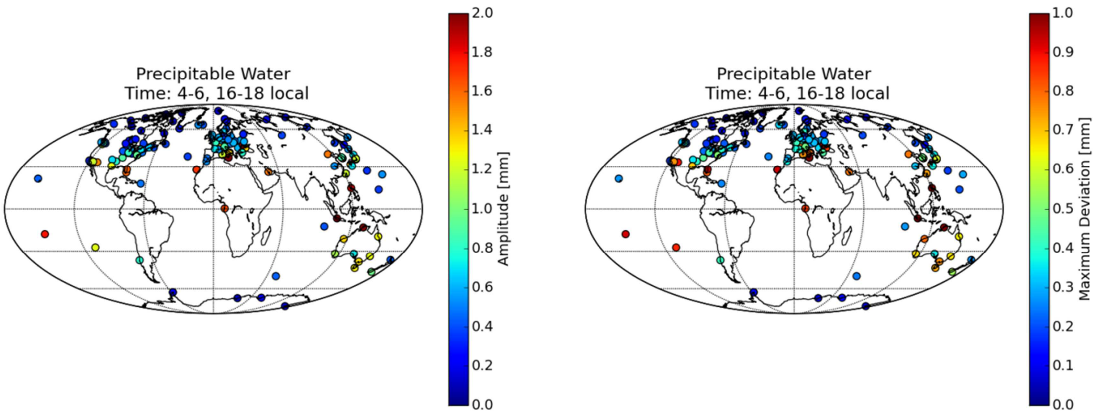

Figure 7. Amplitude (left) and maximum deviation (right) scale.

Figure 7 reveals, as expected from the investigation of single stations in section 4.2.1., a zonal dependency. Maritime stations tend to have lower values than continental stations on the same latitude.
Relative values of amplitude and maximum deviation are presented in the appendix, section 8.4, while seasonal plots demonstrating can be found in section 8.5.

4.3.3 Local minimum and maximum times

This section shows the times, where the absolute minimum and maximum times of the diurnal cycle occur (Figure 8).
The minimum value is found usually in the morning hours, between 7 and 11 LST. Nevertheless a few outliers can be found, for example in the Rocky Mountains, where the minimum is shifted to afternoon. Some randomly distributed stations reveal their minimum to be at evening or night times.
The maximum usually occurs at evening and night. Again, the Rocky Mountain stations are delayed, their maximum is shifted to early morning hours.
The resulting time difference usually is 8 to 12 hours, while a few stations have only 6 hours in between.

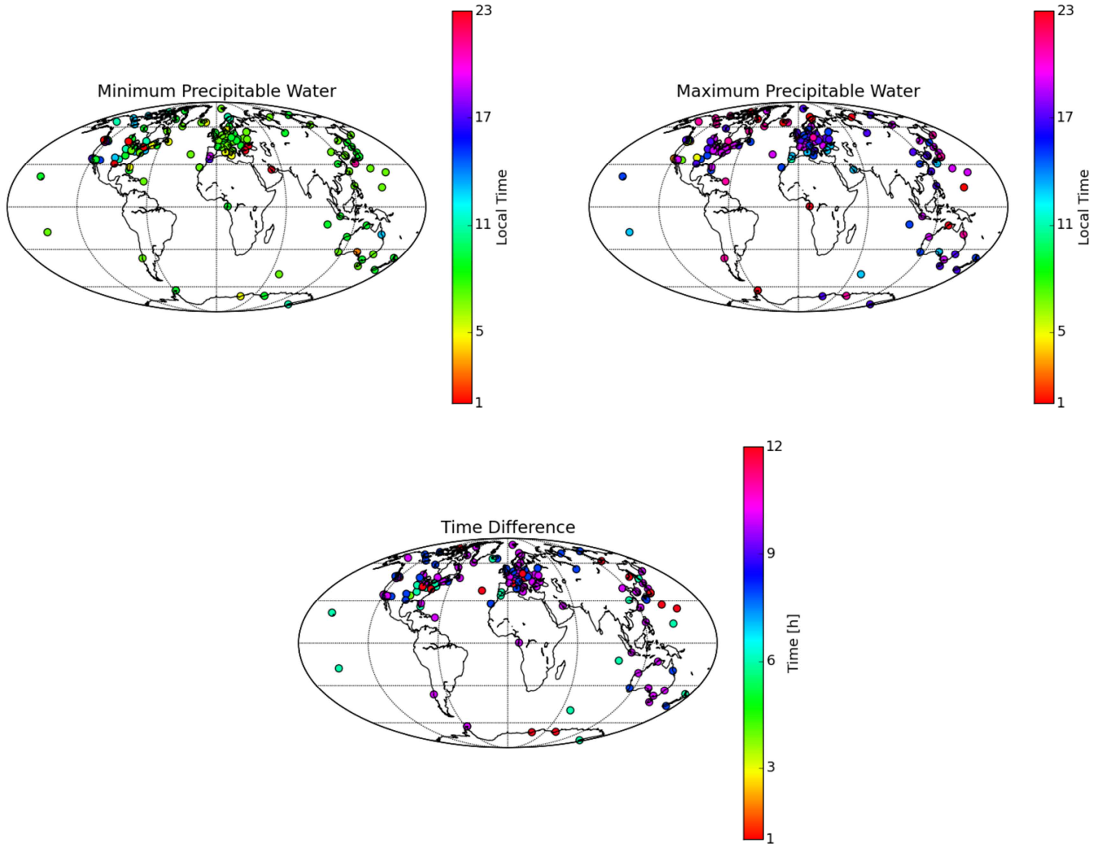

Figure 8. Local time of minimum (upper left) and maximum (upper right) precipitable water and the resulting time difference (bottom).

Figure 9 shows the seasonal cycle of the time difference between maximum and minimum diurnal cycle.

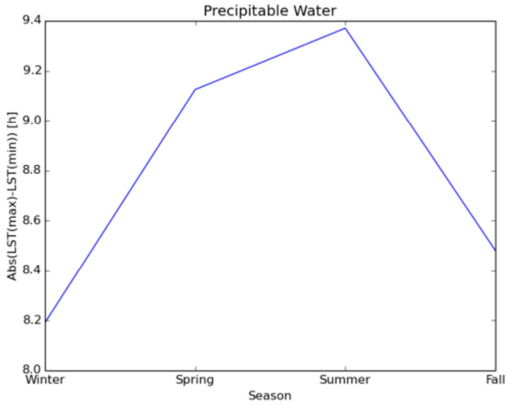

Figure 9. Time difference between minimum and maximum as a function of season.

4.4 Diurnal sampling bias

This section about the bias of distinct overflight times gives the main information about the error of using only two measurements per day to calculate a daily mean value. For classification, the bias is marked as significant in spatial maps. The figures are limited to the climatology instead of a seasonal investigation (see Fig. 10). Here figure 10 shows the climatology while seasonal results are presented in the appendix (Section 8.7).

Figure 10 exposes a tendency to positive biases, however no zonal dependency is obvious. The only tendency is visible in higher latitudes, where the bias is between -0.08 and 0.08. This can be expected from the weak diurnal cycles in these regions.

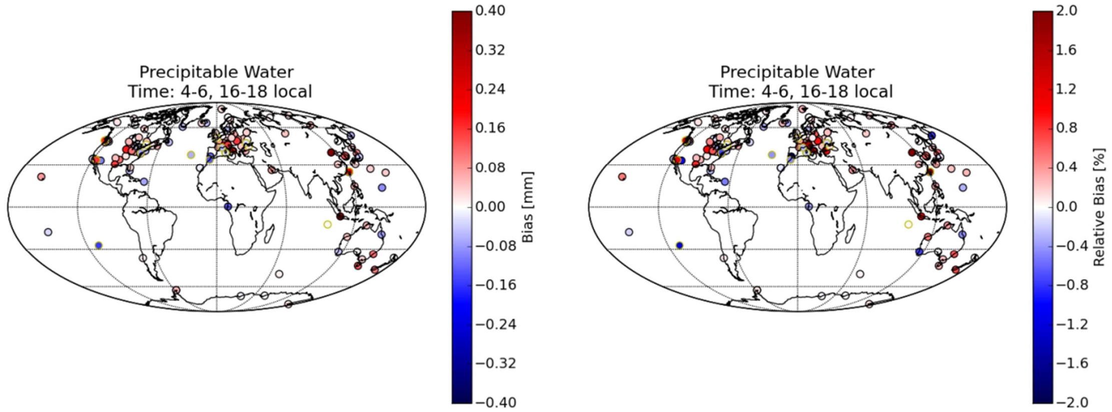

Figure 10. Absolute (left) and relative (right) bias of precipitable water. Yellow circles indicate a significant bias.

The largest bias is exposed by station *BAKO* (see section 4.2.1). As discussed already, this station has a distinct but compressed sinusoidal shape. Therefore a large bias is expected.

Further investigations of the bias reveals no dependency on mean, latitude and amplitude as well as a dependency of the time-amplitude factor (see appendix, section 8.9). The probability density functions are also not showing any dependency (see appendix, section 8.8).

Figure 11 shows the diurnal cycle of the bias as a function of LST bins and pairs of LST bins in absolute and relative units. The largest bias occurs by combining the 2-4 LST with 14-16 LST bins while the smallest bias occurs by using the bins 6 hours later. Figure 11 also explains why figure 7, using the 4-6 and 16-18 LST bins, tends to exhibit positive biases.
Separated by the seasons the diurnal cycles reveal a similar behaviour, however the minimum and maximum times are slightly varying as well as the amplitude. This causes a minor difference in the bias as seen in section 8.6 (Appendix). The tendency to positive biases as well as the dependency on height is visible.

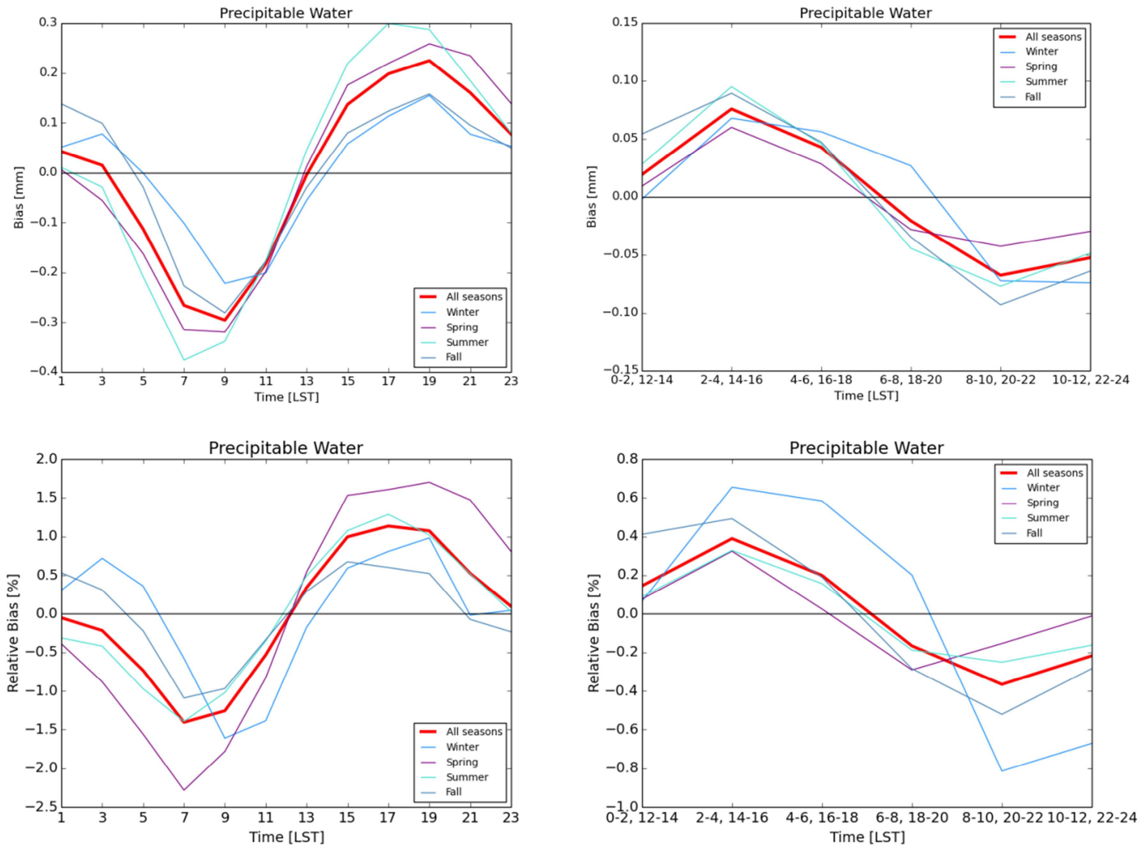

Figure 11. Diurnal cycle of the bias and the resulting diurnal cycle for combined overflight times in absolute (top) and relative (bottom) values.

Figure 12 shows that the bias decreases if several satellites are used. The decrease is about linear and it is difficult to give a threshold of how many satellites should be used for a reasonable climatology, however, combining figure 12 with figure 11 exposes two satellites are reasonable in case their overflight times differ by 6 hours.

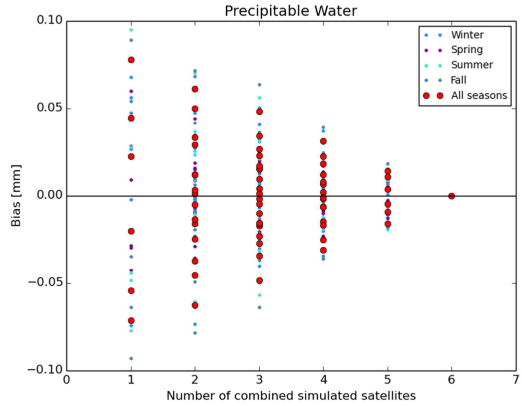

Figure 12. Bias of combined overflight times simulating a satellite passing twice a day (left) and the number of combined simulated satellites (right).

4.5 Diurnal sampling standard deviation

Here the impact of temporal sampling on the standard deviation is described. A dependency of standard deviation from latitude is obvious (see figure 13), with the largest standard deviation measured by the Indonesian station *BAKO*. Recall, this station was already displaying the largest bias and one of the largest means as well as amplitude. Figure 13 additionally reveals a dependency on altitude, which decreases the standard deviation slightly.

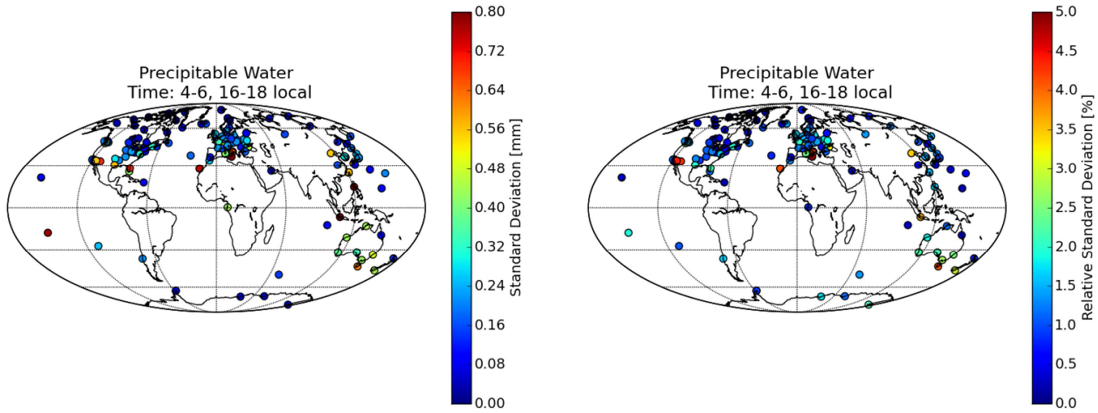

Figure 13. Absolute (left) and relative (right) standard deviation of precipitable water.

As expected from the dependency of standard deviation from amplitude, which itself was found depending on latitude (see section 4.2.1 and 4.4), the seasonal investigation reveals a distinct annual cycle (Figure 14, Appendix section 8.10): The standard deviation is large in summer and low in winter.

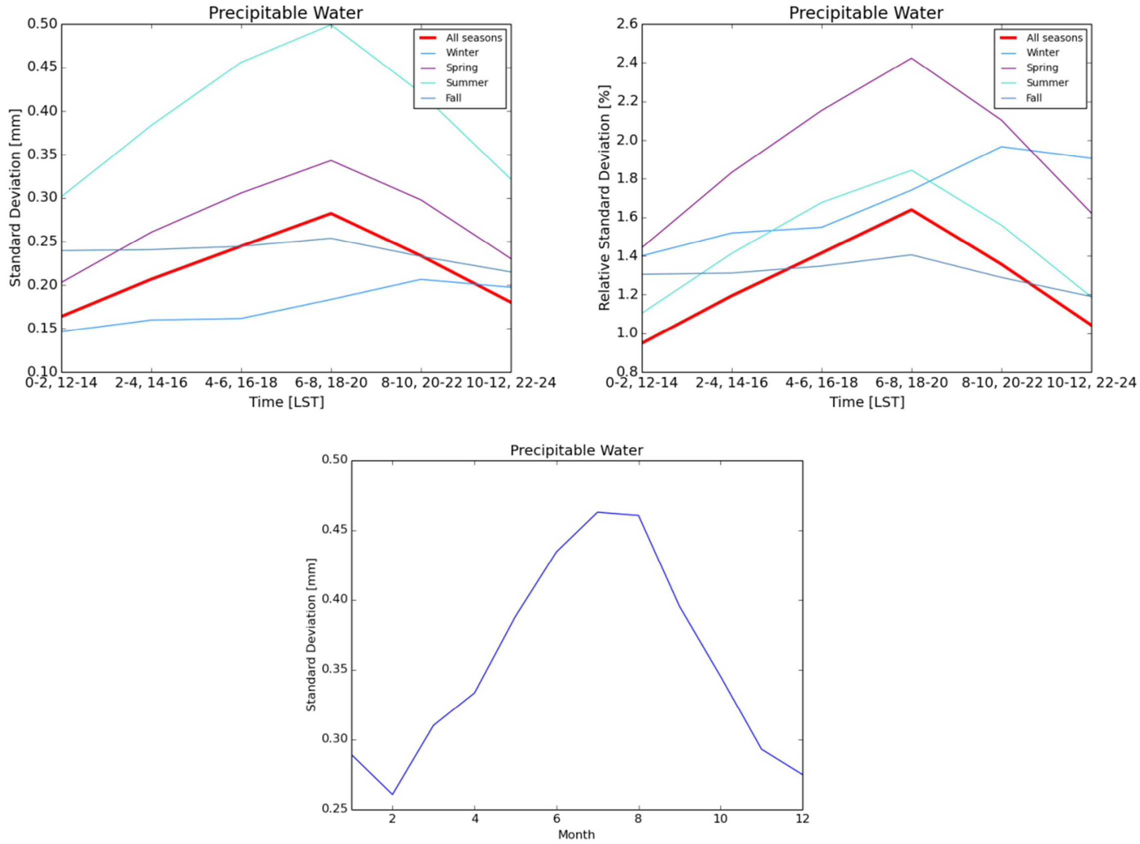

Figure 14. Absolute (upper left) and relative (upper right) diurnal cycle of standard deviation as well as the annual cycle (bottom). Note: Only stations from northern hemisphere were taken into account.

Figure 15 adds two other dependencies to this investigation of standard deviation. Figure 15 shows a scatterplot of standard deviation and amplitude as well as time-amplitude-factor. The correlation to amplitude is 0.85 and larger than for the time-amplitude-factor case.

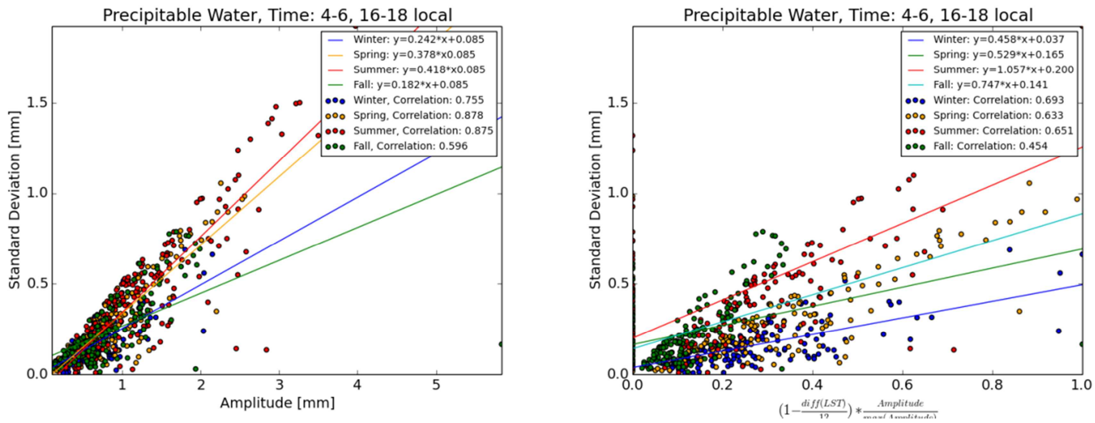

Figure 15. Correlation between standard deviation and amplitude (left) as well as time-amplitude-factor (right).

Other relations are shown in the appendix, see section 8.13 (appendix).

Similar to the bias, the standard deviation decreases if more and more satellites are combined (see figure 16).

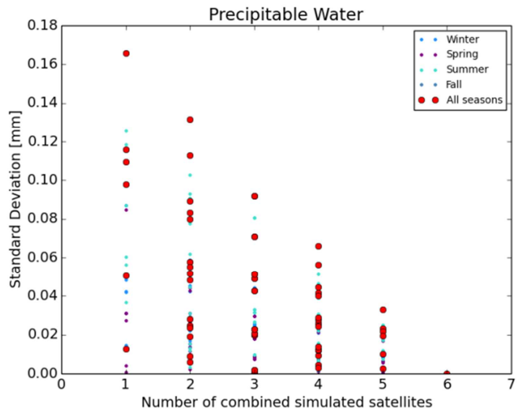

Figure 16. Number of simulated satellites that pass twice a day versus the standard deviation.

Relative standard deviations are given in the Appendix, section 8.11.

5 Conclusions

This study uses the precipitable water of the 2-hourly global NCAR/NCEP GNSS data base of a 5-year-period to provide a general overview of the climatological diurnal cycle. The potential impact of this diurnal cycle on the quality of satellite observations has been analysed by considering pairs of LST bins.

The diurnal cycle is described in terms of amplitude, LST of minimum and maximum precipitable water as well as the time difference between the occurrence of minimum and maximum. The minimum of the diurnal cycle occurs usually in the morning, while the maximum occurs mostly in late afternoon. This results in a time difference of about 10 hours and thus to a compressed sinusoidal shape. This is altered by altitude, which delays minimum and maximum by a few hours. Noticeable is the low relative amplitude at maritime and therefore low-altitude stations. The features mentioned above are resulting in a compressed sinusoidal diurnal cycle which might cause a bias if a diurnal cycle is present and insufficiently sampled, i.e. only two times per day.

The observed bias and standard deviation between climatology and simulated satellite overpass exhibits a strong spatial variability. However, overall absolute and relative values are small. The bias as a function of pairs of LST bins exhibits a diurnal cycle with minimum and maximum values at 2-4, 14-16 LST and 8-10, 20-22 LST, respectively. Northern hemispheric averages do not exceed values of -0.1 mm and -1 %. Thus, its impact on the bias is small. It might however be of relevance if data affected by temporal sampling are used for climate analysis.

Also, the investigation of the bias revealed that the bias is independent from latitude and the chosen overflight times. The bias is largely reduced when two satellites with 6 hours time shift are operated.

The standard deviation strongly depends on the annual cycle and the latitude.

The bias observed among major precipitable water climate data records are much larger than the temporal sampling bias described here. We argue that the biases are not primarily caused by a diurnal cycle of precipitable water but by sampling the clear sky bias caused by the diurnal cycle of clouds and the change in sampling in vis and IR based retrievals.

Finally, some stations were found to be peculiar and some data in December missing. This has been communicated to the NCAR GNSS data record PI.

6 Acknowledgement

This work was supported by the European Space Agency (ESA) projects EMiR and GOME EVL. J. Wang (now at Albany University) kindly provided the NCAR GNSS precipitable water data record.

7 References

Bevis, M., S. Businger, T.A. Herring, C. Rocken, R.A. Anthes, R.H. Ware (1992), GPS Meteorology: Remote Sensing of Atmospheric Water Vapor Using the Global Positioning System, J. Geophys. Res., 97(D14), 15787-15801.

Bordi, I, R. De Bonis, K. Fraedrich, A. Sutera (2015), Interannual variability patterns of the world's total column water content: Amazon River Basin, Theoretical and Applied Climatology, 122(3-4), 441-455, doi: 10.1007/s00704-014-1304-y.

Dai, A., J. Wang, R. H. Ware, and T. Van Hove (2002), Diurnal variation in water vapor over North America and its implications for sampling errors in radiosonde humidity, J. Geophys. Res., 107(D10), doi:10.1029/2001JD000642.

Hanesiak, J., M. Melsness, R. Raddatz (2010), Observed and Modeled Growing-Season Diurnal Precipitable Water Vapor in South-Central Canada, J. Appl. Meteor. Climatol., 49, 2301-2314, doi: 10.1175/2010JAMC2443.1.

Jin, S., O.F. Luo (2009), Variability and Climatology of PWV From Global 13-Year GPS Observations, IEEE Transactions on Geoscience and Remote Sensing, 47(7), 1918-1924, doi: 10.1109/TGRS.2008.2010401.

Ningombam, S.S., S. Jade, T.S. Shrungeshwara, H.-J. Song (2016), Validation of water vapor retrieval from Moderate Resolution Imaging Spectro-radiometer (MODIS) in near infrared channels using GPS data over IAO-Hanle, in the trans-Hilalayan region, J. of Atmos. And Solar-Terrestrial Phys., 137, 76-85, doi: 10.1016/j.jastp.2015.11.019.

Ortiz de Galisteo, J.P., V. Cachorro, C. Toledano, B. Torres, N. Laulainen, Y. Bennouna, A. de Frutos (2011), Diurnal cycle of precipitable water vapor over spain, Quarterly Jounal of the Royal Meteorological Society, 137(657), 948-958, doi: 10.1002/qj.811.

Radhakrishna, B., F. Fabry, J.J. Braun, T. Van Hove (2015), Precipitable Water from GPS over the Continental United States: Diurnal Cycle, Intercomparisons with NARR, and Link with Converctive Initiation, J. Climate, 28, 2584-2599, doi: 10.1175/JCLI-D-14-00366.1.

Rocken, C., R. Ware, T. Van Hove, F. Solheim, C. Alber, J. Johnson, M. Bevis, S. Businger (1993), Sensing atmospheric water vapor with the global positioning system, Geophys. Res. Lett., 20(23), 2631-2634, doi: 10.1029/93GL02935.

Rocken, C., T. Van Hove, J. Johnson, F. Solheim, R. Ware, M. Bevis, S. Chiswell, S. Businger (1995), GPS/STORM – GPS Sensing of Atmospheric Water Vapor for Meteorology, J. Of Atm. And Ocean. Tech., 12(3), 468-478, doi: 10.1175/1520-0426(1995)012<0468:GSOAWV>2.0.CO;2.

Wang, J., L. Zhang, A. Dai, T. van Hove, and J. Van Baelen (2007), A near-global, 2-hourly data set of atmospheric precipitable water from ground-based GPS measurements, J. Geophys. Res., 112, D11107, doi:10.1029/2006JD007529.

Wang, J., L. Zhang (2008), Systematic Errors in Global Radiosonde Precipitable Water Data from Comparisons with Ground-Based GPS Measurements, J. Climate, 21, 2218-2238, doi: 10.1175/2007JCLI1944.1.

Wu, P., J.-I. Hamada, S. Mori, Y.I. Tauhid, M.D. Yamanaka, F. Kiruma (2003), Diurnal Variation of Precipitable Water over Mountainous Area of Sumatra Island, J. Appl. Meteor., 42, 1107-1115, doi: 10.1175/1520-0450(2003)042<1107:DVOPWO>2.0.CO;2.

Yu, H., P.E. Ciesielski, J. Wang, H.-C. Kuo, H. Vömel, R. Dirksen (2015), Evaluation of Humidity Correction Methods for Vaisala RS92 Tropical Sounding Data, J. Atmos. Oceanic Technol., 32, 397-411, doi: 10.1175/JTECH-D-14-00166.1.

8 Appendix

8.1 List of data availability

Table 1. Number of stations with more than 75% of data in a 5 year period.

Time Period	Number of Years	Number of Stations
1995-1999	5	0
1996-2000	5	12
1997-2001	5	17
1998-2002	5	40
1999-2003	5	49
2000-2004	5	75
2001-2005	5	99
2002-2006	5	114
2003-2007	5	134
2004-2008	5	179
2005-2009	5	148
2006-2010	5	146
2007-2011	5	146

8.2 List of peculiar stations

This list shows the diurnal cycles of precipitable water, temperature and pressure to give a general overview. All figures are structured in the same way: precipitable water (left), temperature (middle) and surface pressure (right). Recall, this study is limited to the years 2004 to 2008. For all stations in this list, the 75% threshold was used. All stations listed here were excluded from analysis.

Table 2. List of peculiar stations. Each line presents precipitable water (left), temperature (middle) and pressure (right) of one station.

ASPA

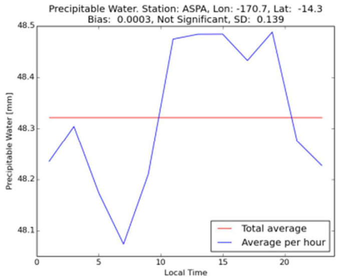

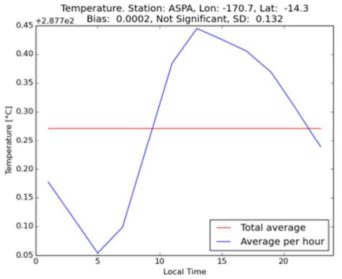

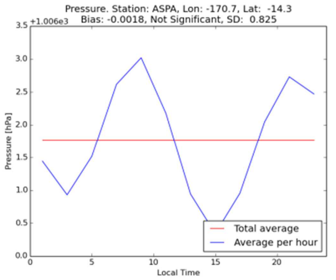

<u>BAIE</u>

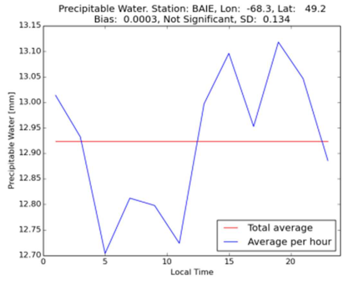

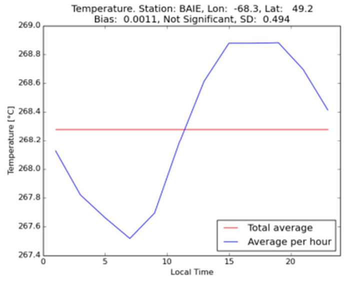

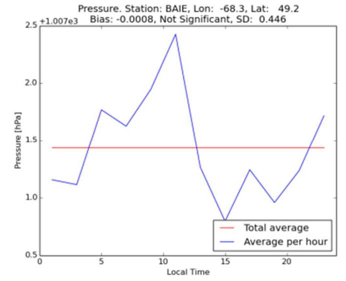

<u>BRMU</u>

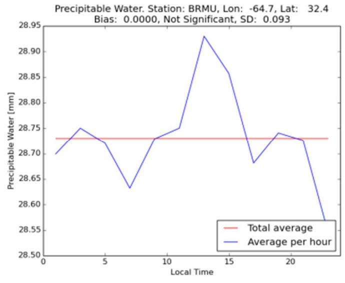

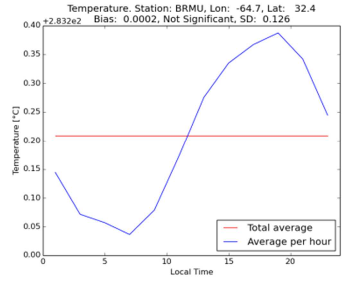

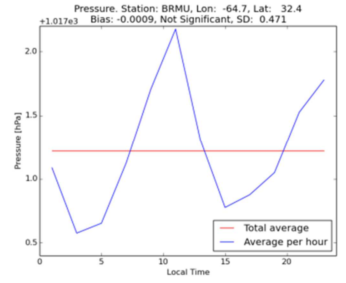

<u>CAS1</u>

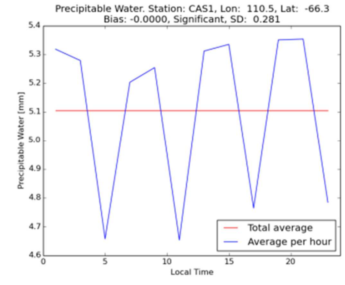

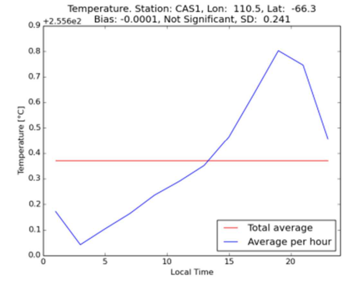

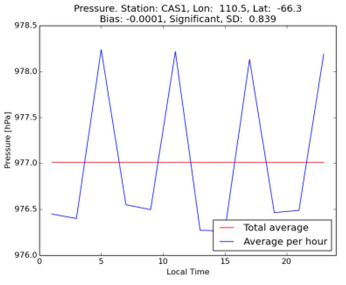

CHAT

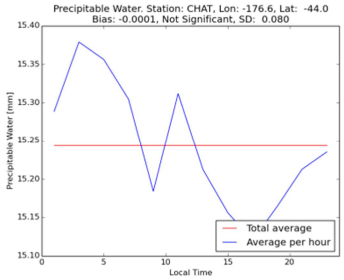

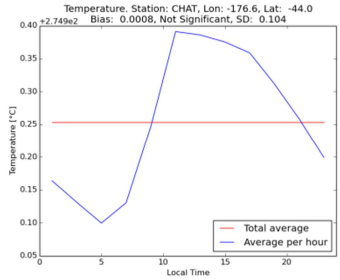

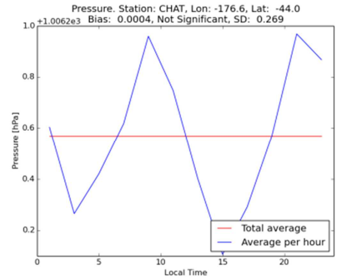

FFMJ

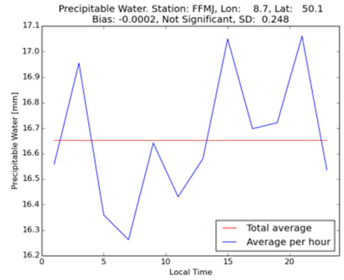

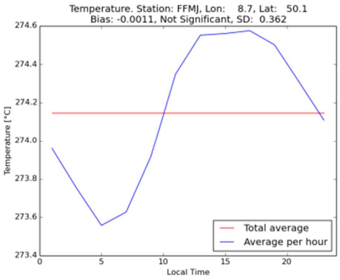

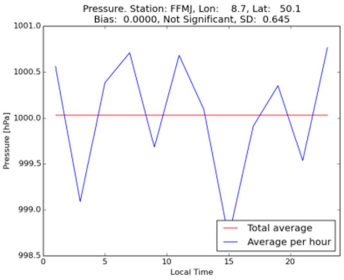

FLIN

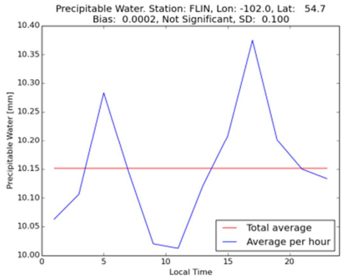

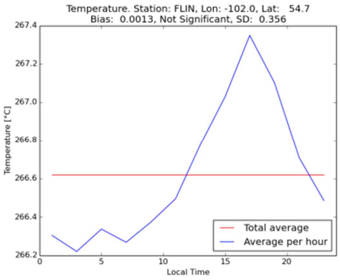

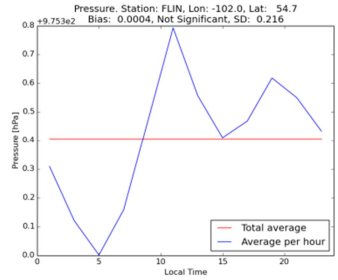

KSMV

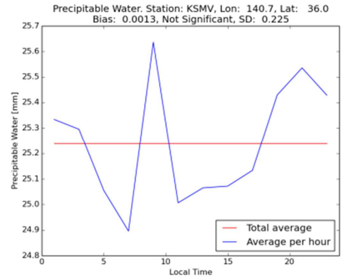

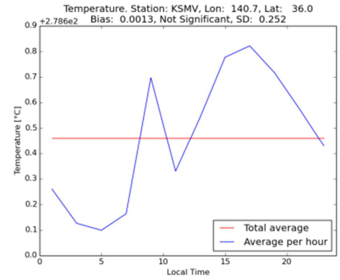

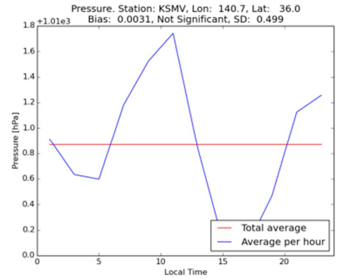

LROC

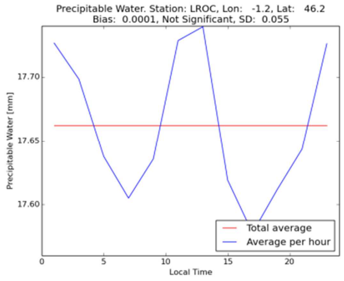

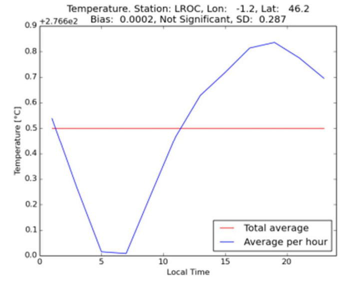

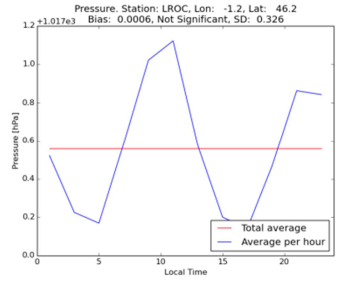

MAC1

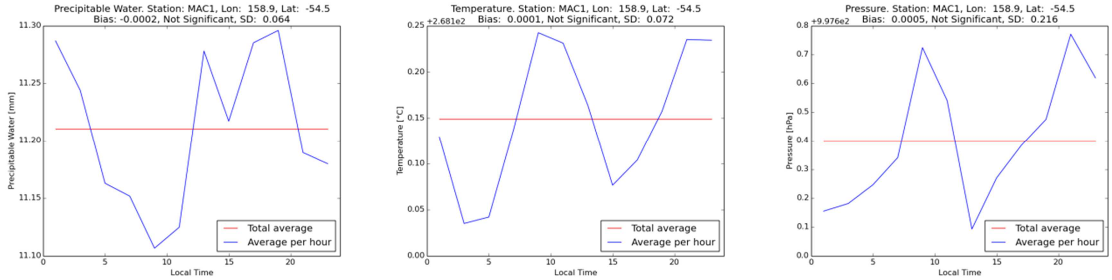

METS

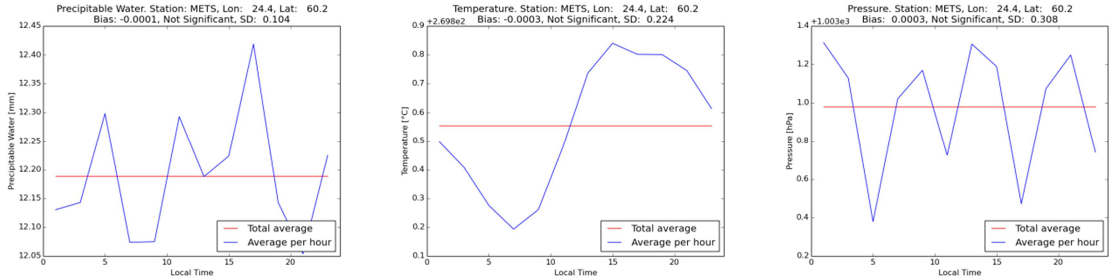

METZ

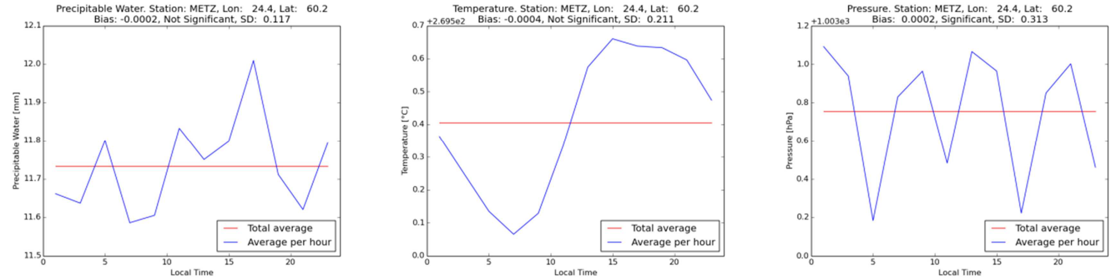

RIGA

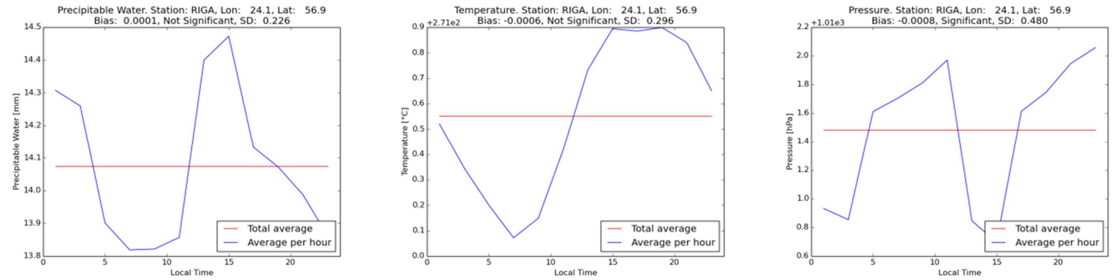

SASS

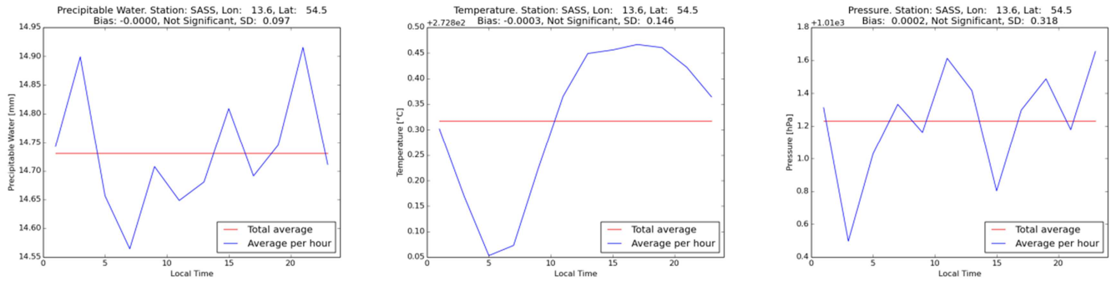

SC04

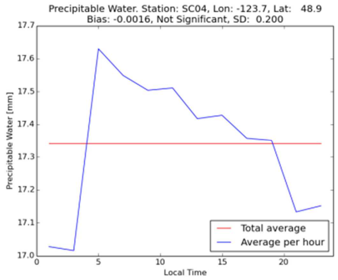

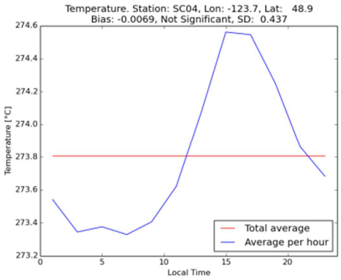

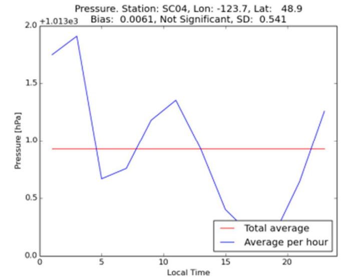

TITZ

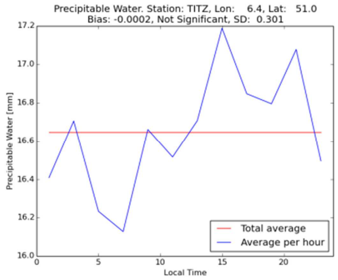

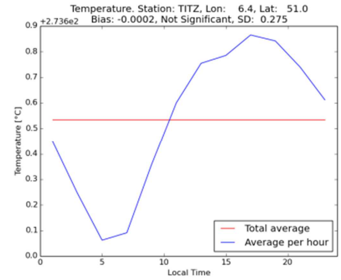

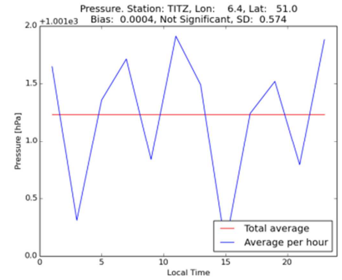

TRAK

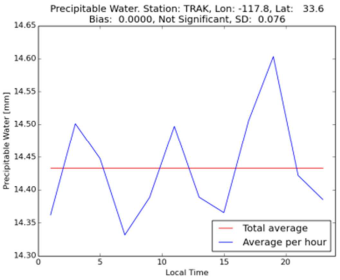

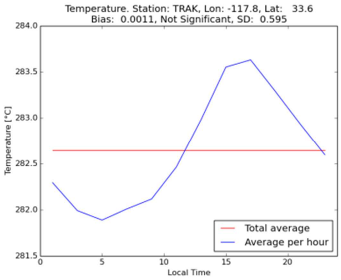

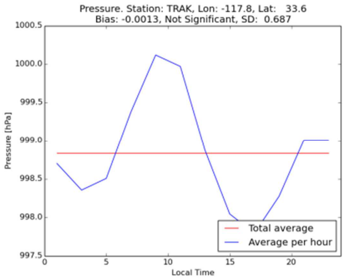

TUKT

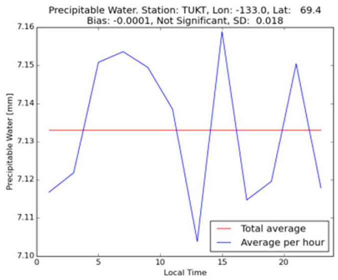

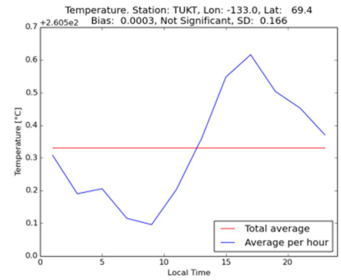

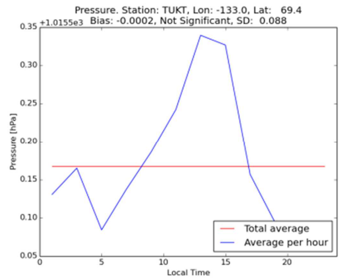

VIS0

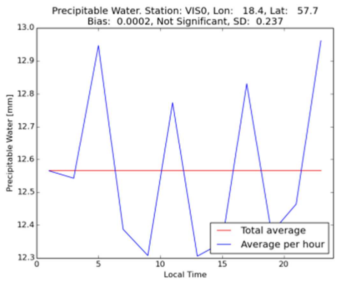

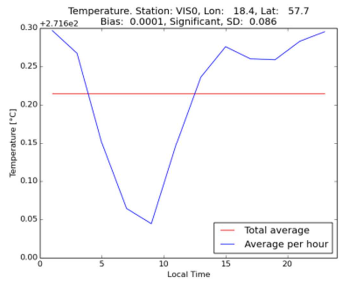

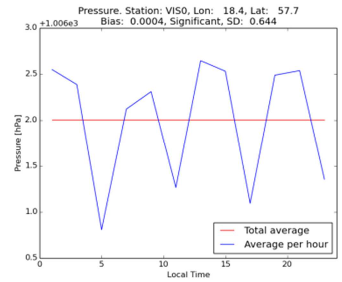

WTZA

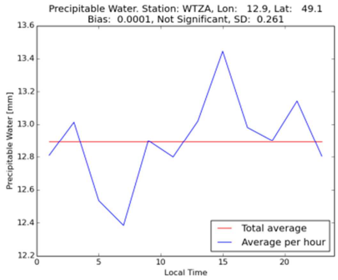

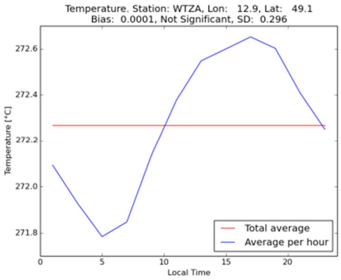

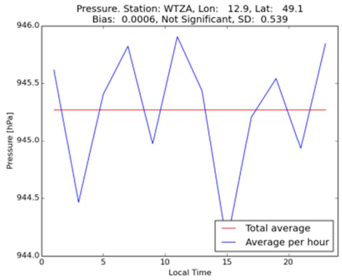

WTZJ

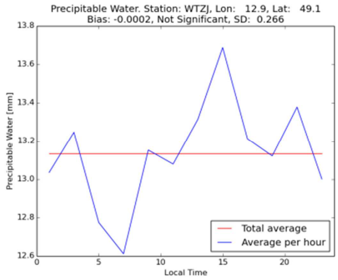

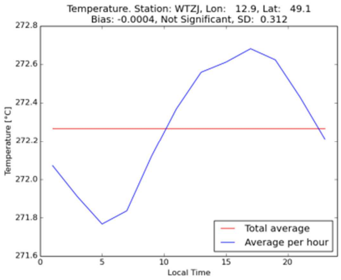

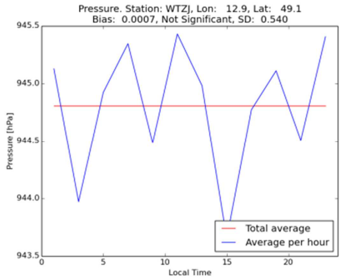

WTZR

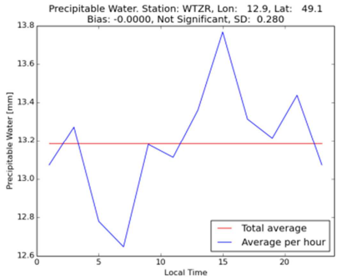

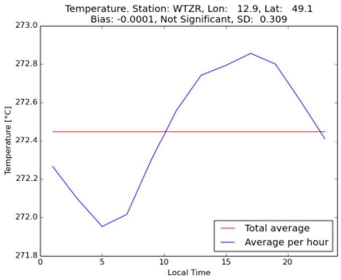

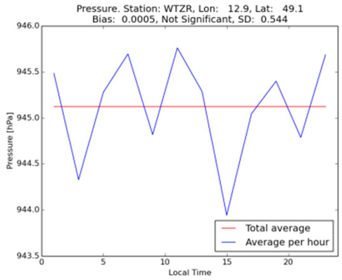

WTZZ

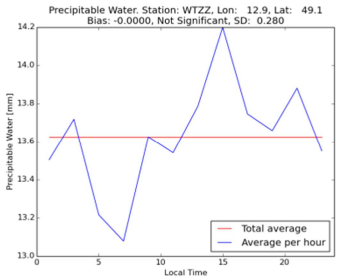

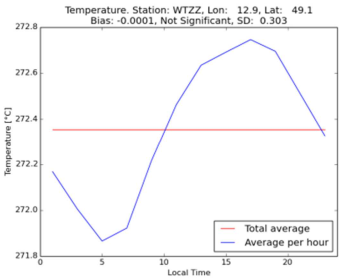

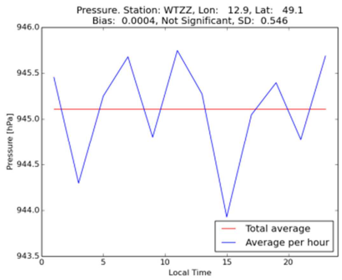

8.3 Relative Diurnal Cycles

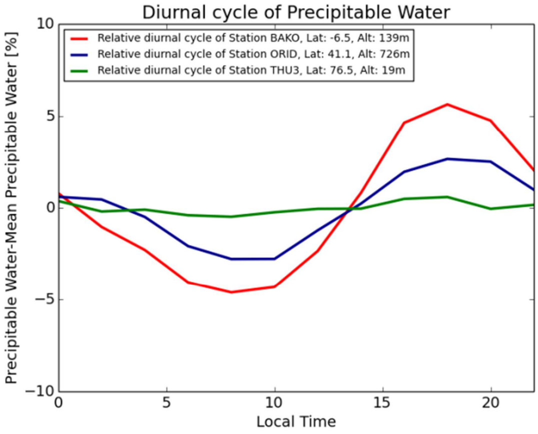

Figure 17. Relative diurnal cycle.

8.4 Relative Amplitude and Maximum Deviation

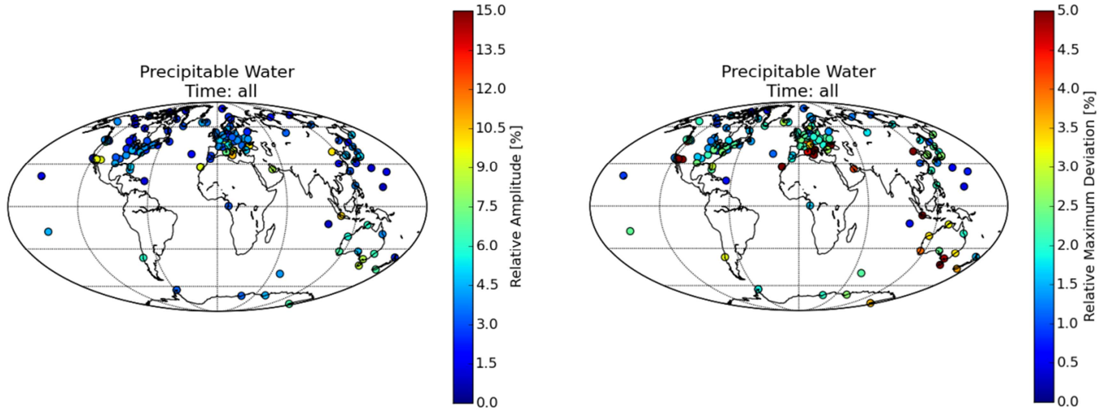

Figure 18. Relative amplitude (left) and maximum deviation (right).

8.5 Seasonal Amplitude and Maximum Deviation

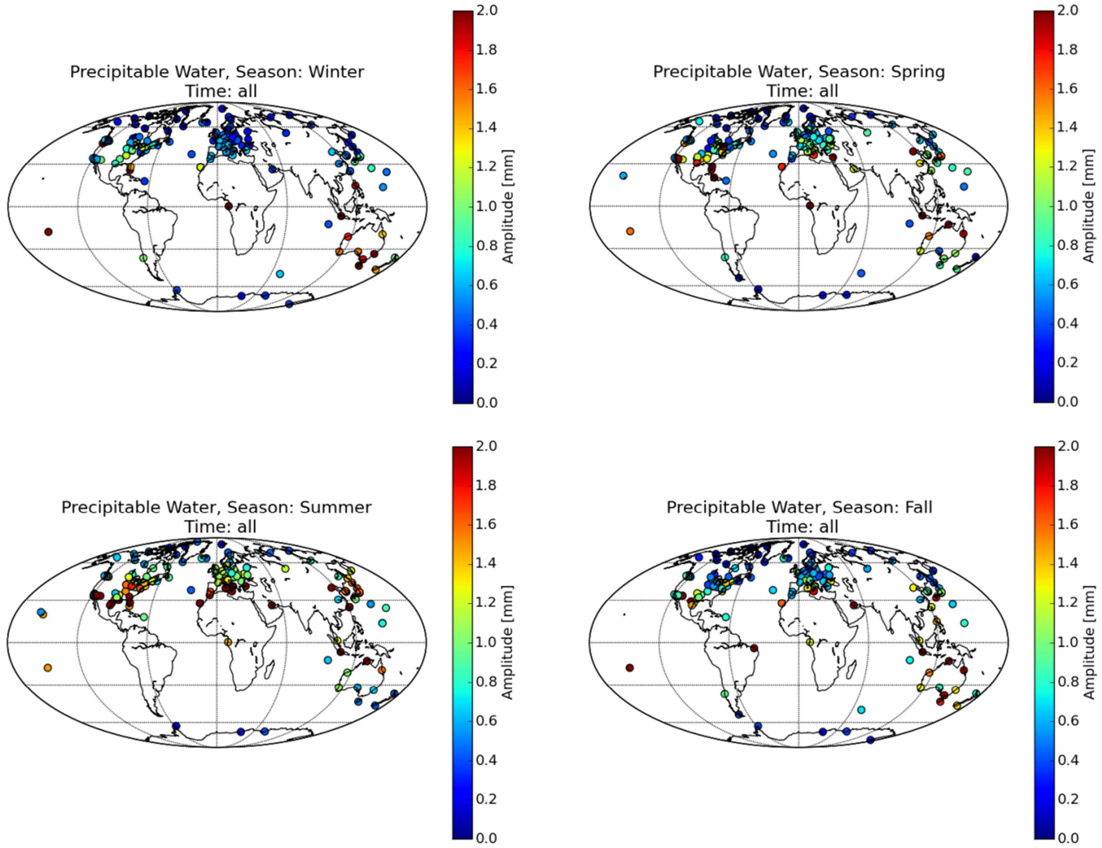

Figure 19. Seasonal amplitude.

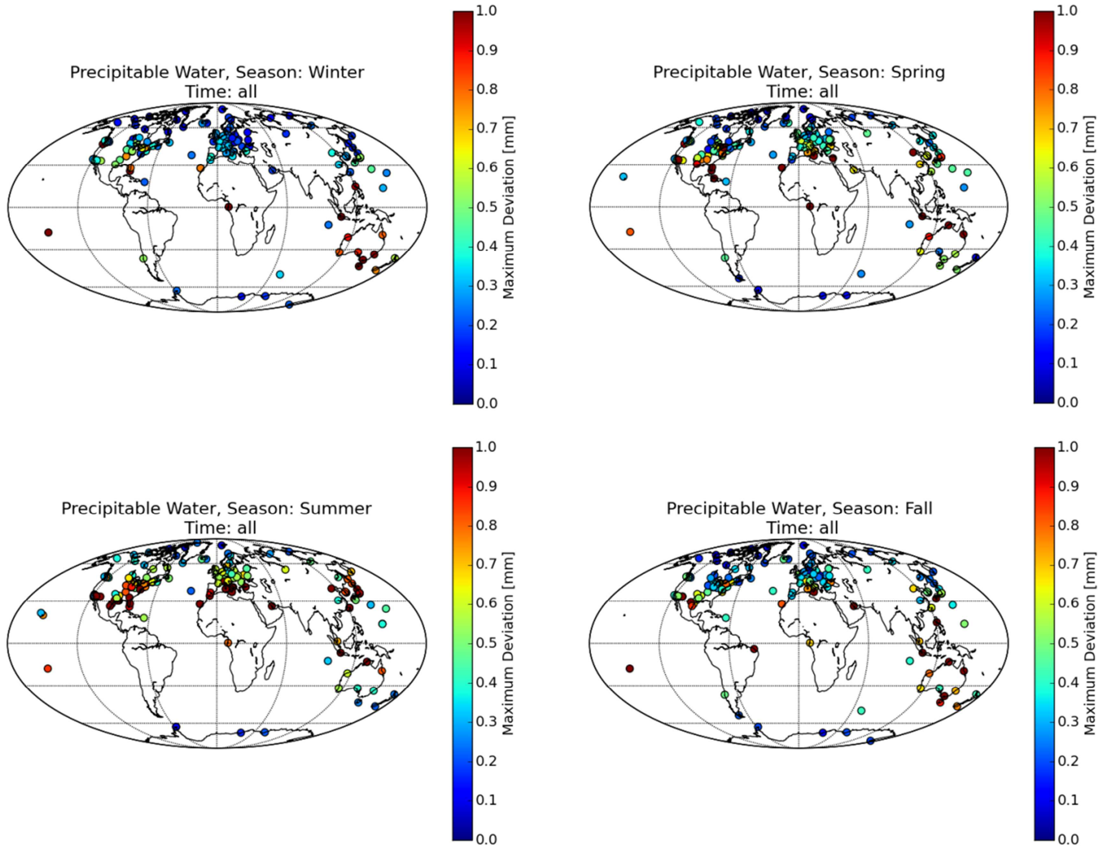

Figure 20. Seasonal maximum deviation.

8.6 Bias: Seasonal

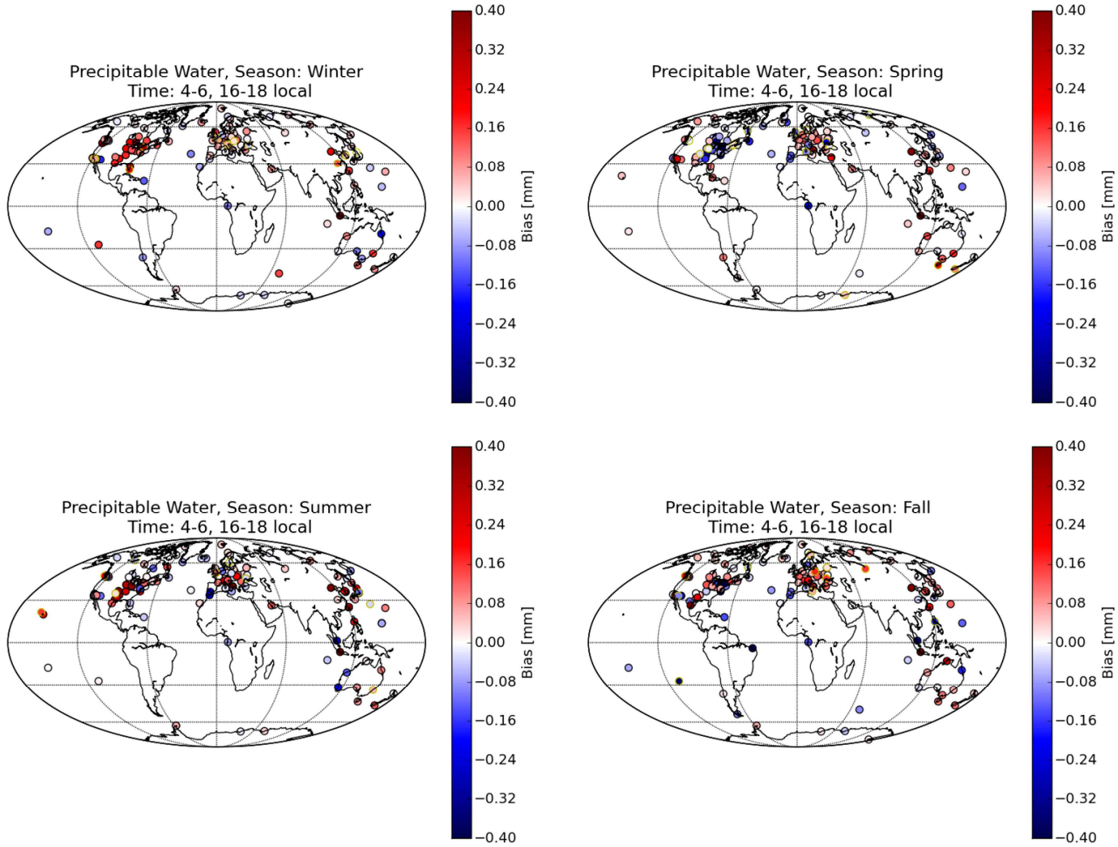

Figure 21. Seasonal bias of January (upper left), April (upper right), July (lower left) and October (lower right).

8.7 Bias: Different overflight times

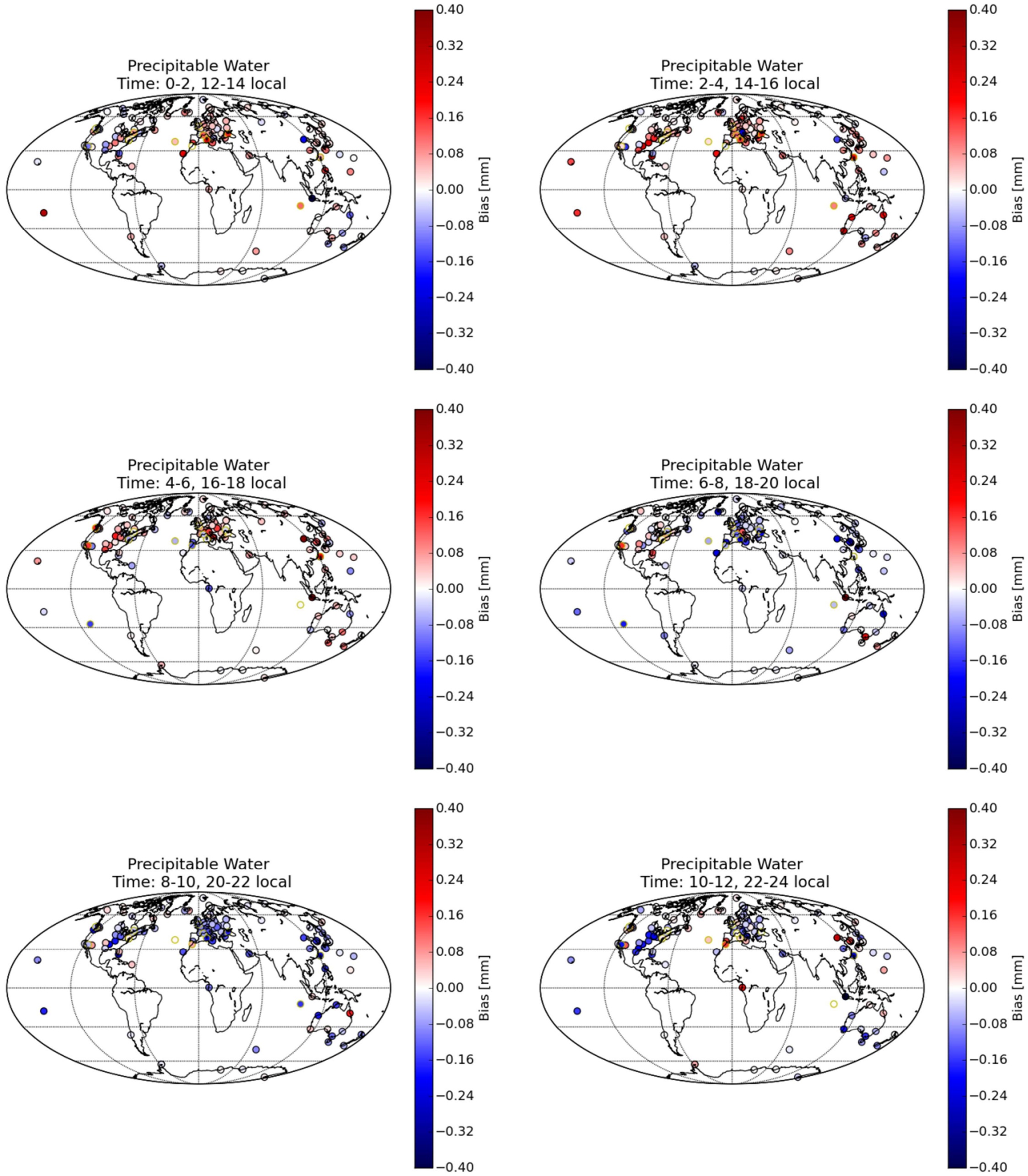

Figure 22. Bias of the total climatology by using only 1 and 13 LST (upper left), 3 and 15 LST (upper right), 5 and 17 LST (middle left), 7 and 19 LST (middle right), 9 and 21 LST (lower left) and 11 and 23 LST (lower right).

8.8 Bias: Probability Density Functions of stations with large bias

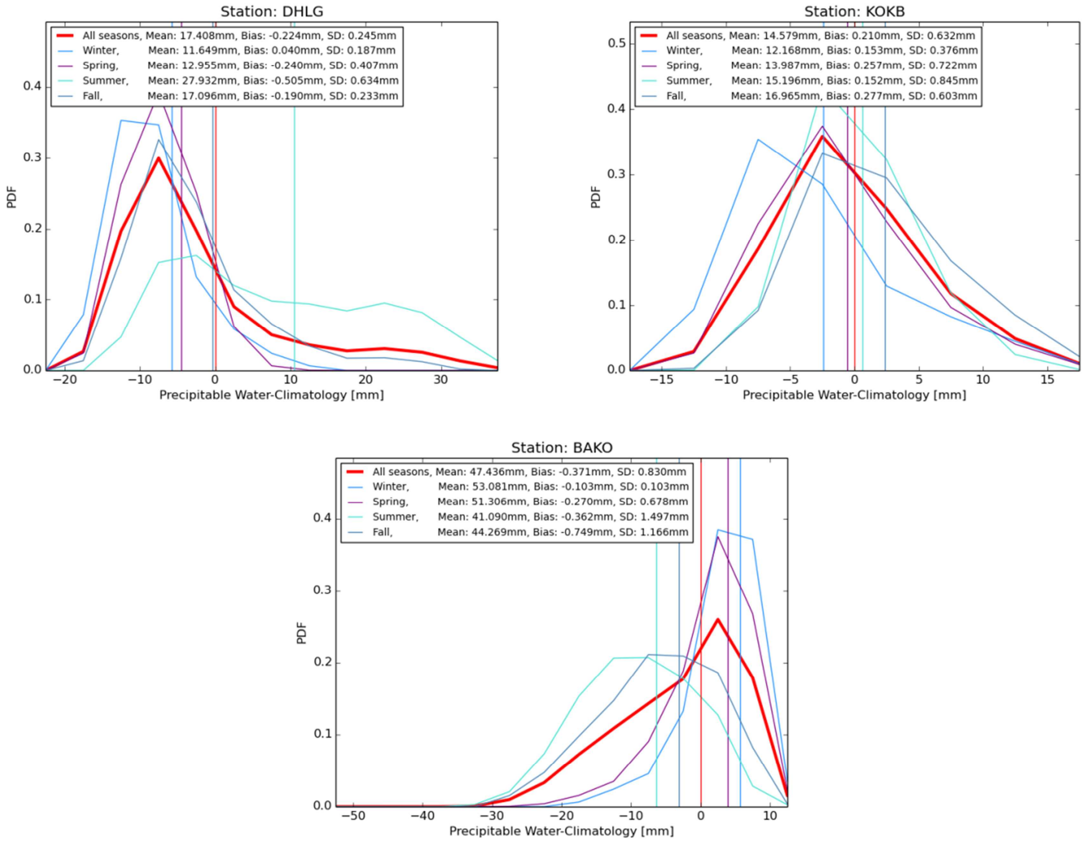

Figure 23. Probability density functions of stations with a large bias.

8.9 Bias: Relations

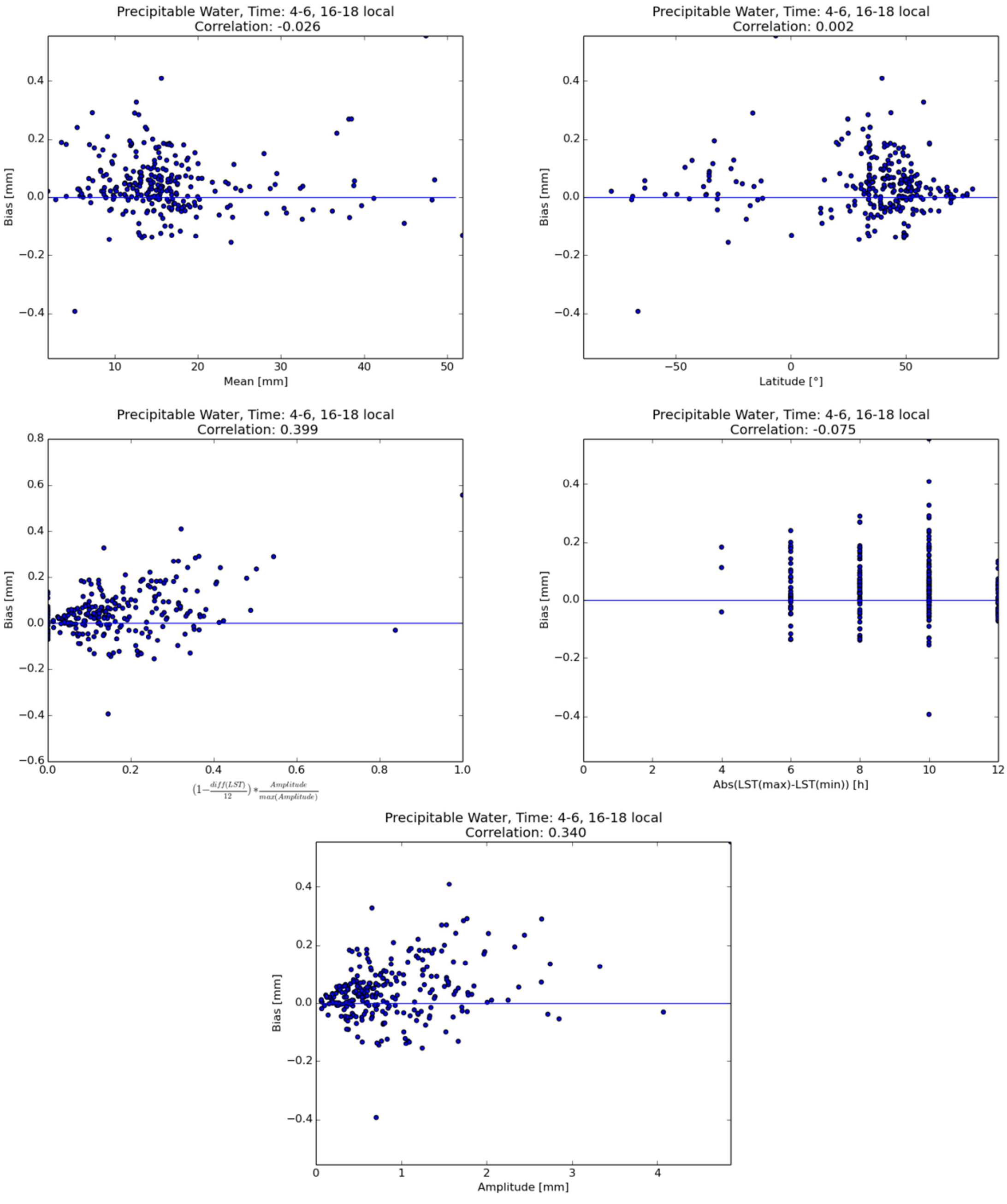

Figure 24. Relations to Bias: Mean (upper left), latitude (upper right), amplitude (middle left), time-amplitude-factor (middle right) and the time difference (bottom).

8.10 Standard deviation: Seasonal

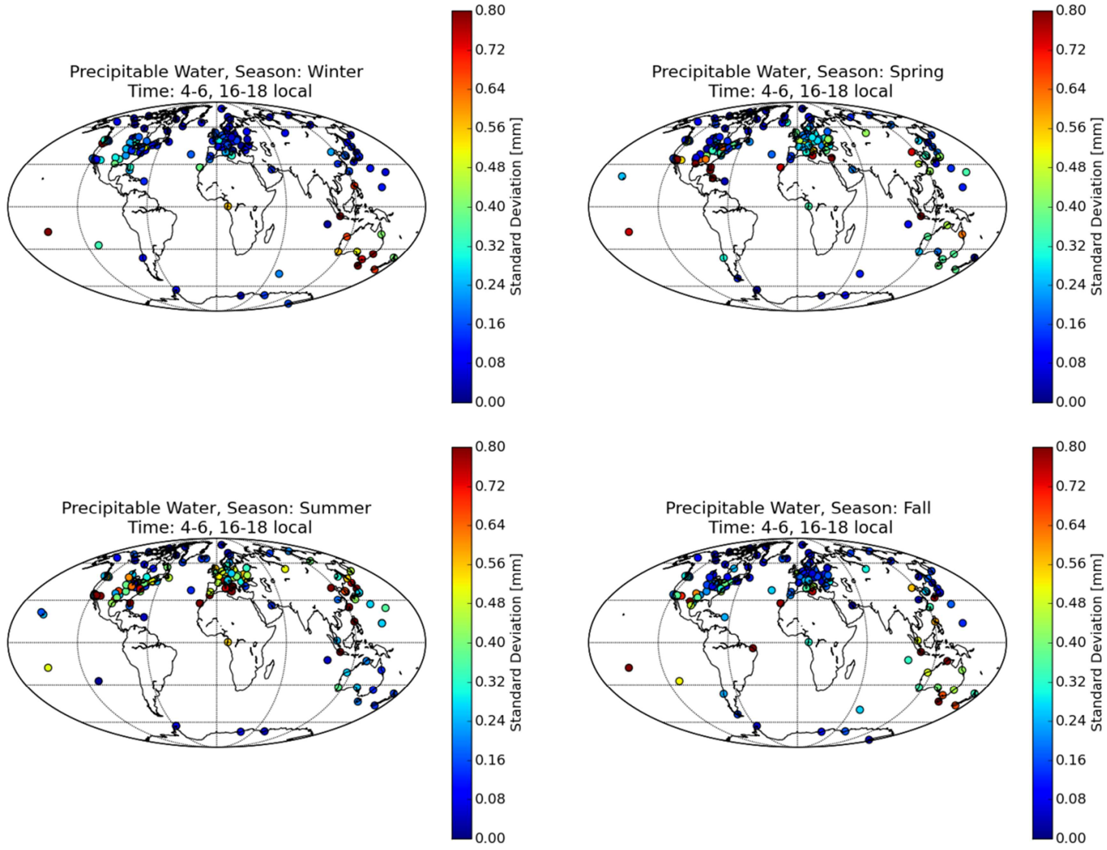

Figure 25. Seasonal standard deviation of January (upper left), April (upper right), July (lower left) and October (lower right).

8.11 Standard deviation: Different overflight times

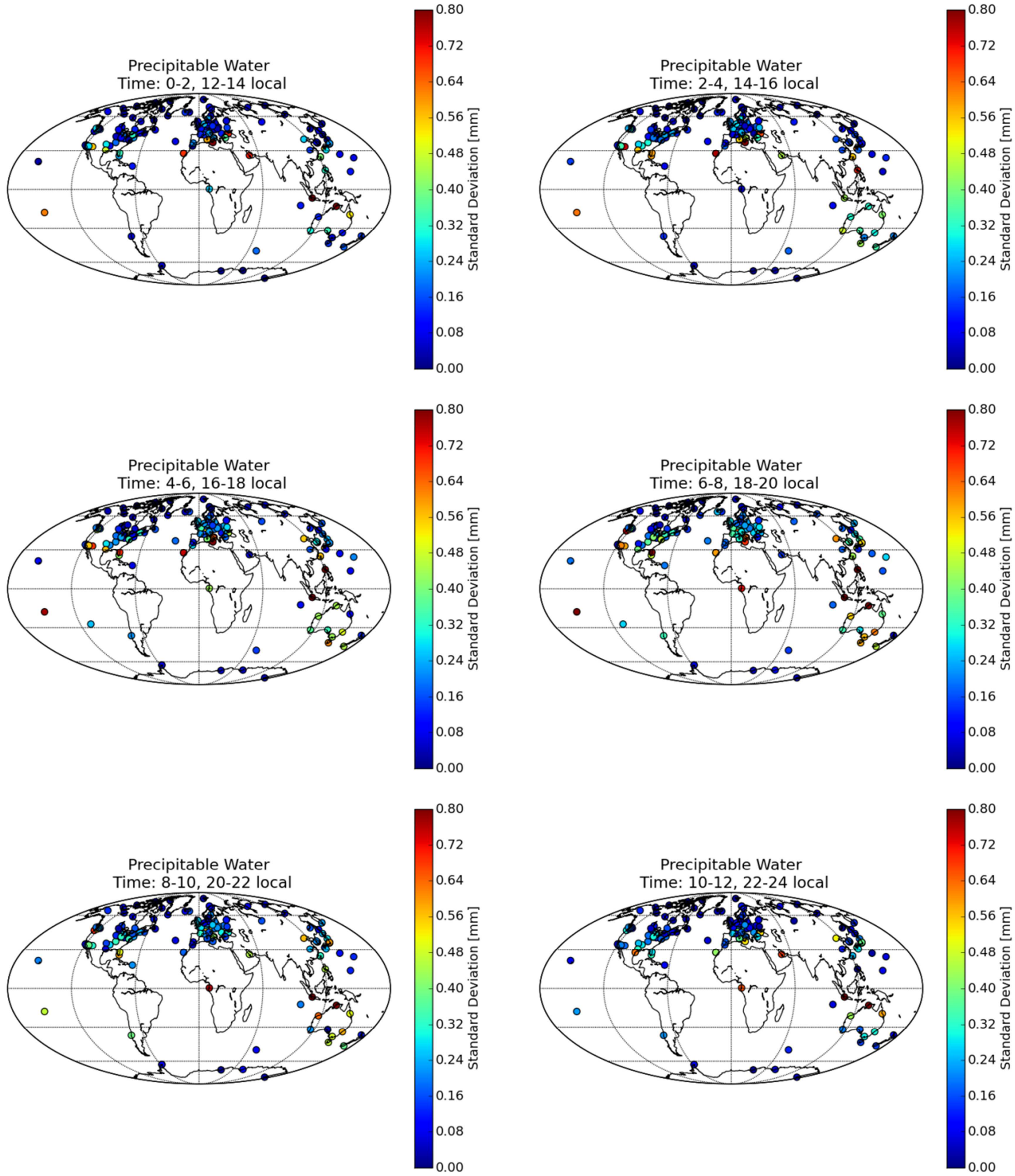

Figure 26. Standard deviation of the total climatology by using only 1 and 13 LST (upper left), 3 and 15 LST (upper right), 5 and 17 LST (middle left), 7 and 19 LST (middle right), 9 and 21 LST (lower left) and 11 and 23 LST (lower right).

8.12 Standard Deviation: Diurnal Cycle

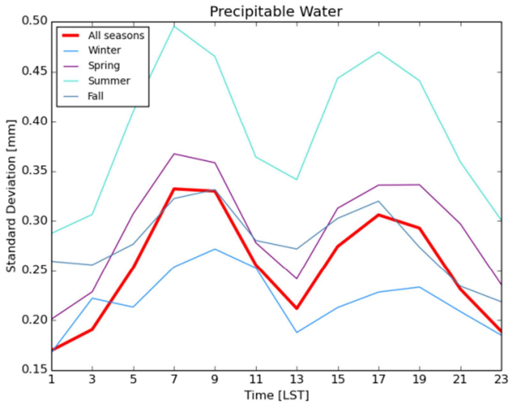

Figure 27. Diurnal cycle of standard deviation for all seasons.

8.13 Standard deviation: Relations

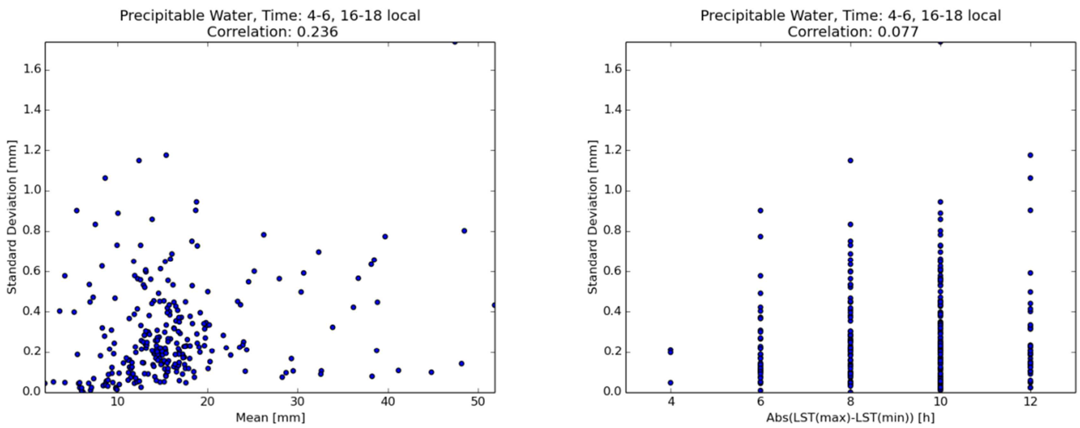

Figure 28. Relation between mean (left) and the time difference between minimum and maximum precipitation (right) of the diurnal cycle versus the standard deviation.

8.14 Relative Values of Bias and Standard Deviation

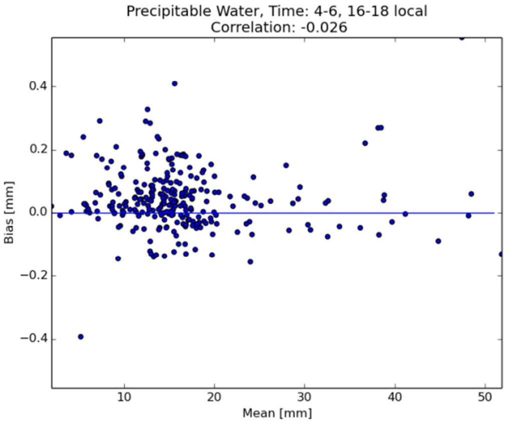

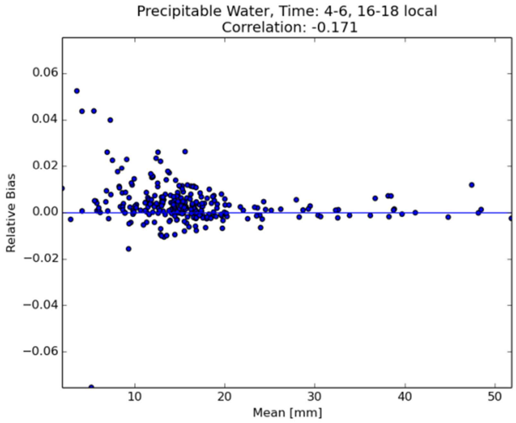

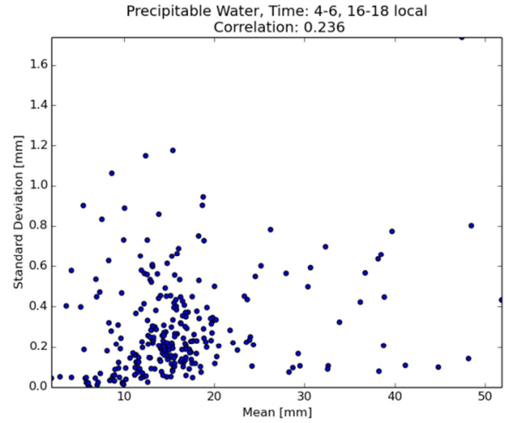

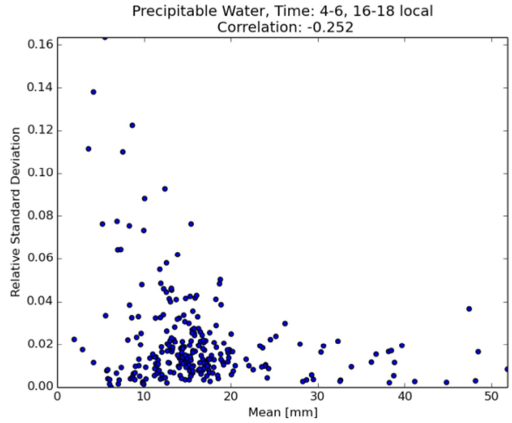

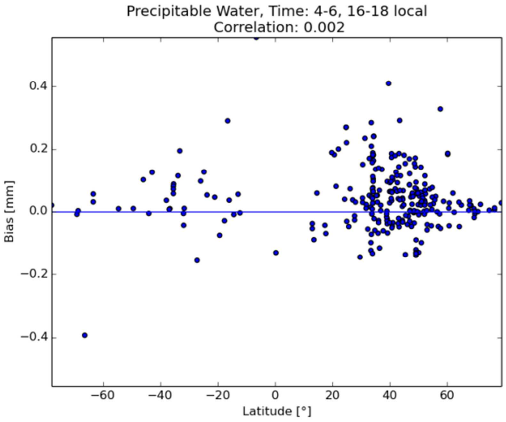

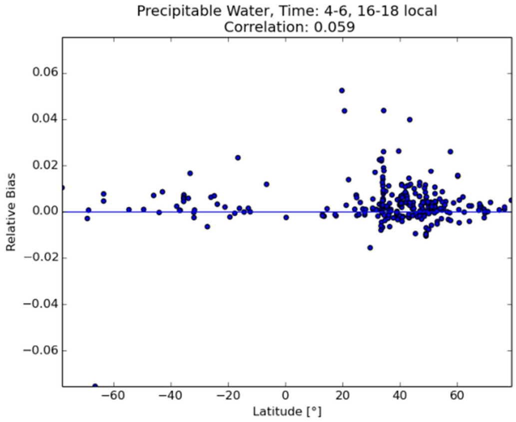

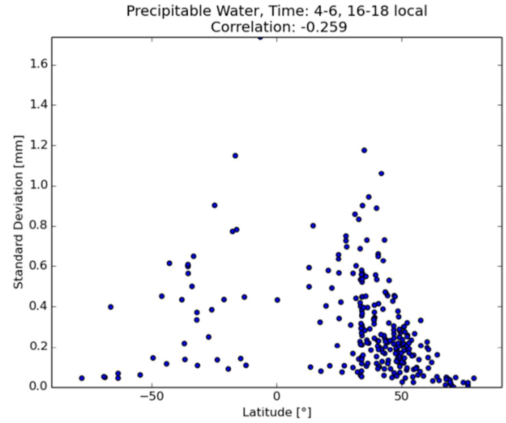

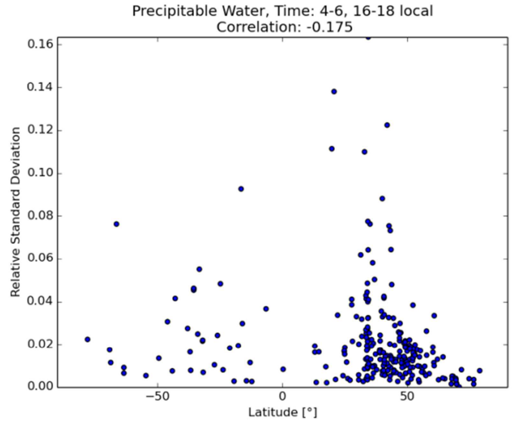

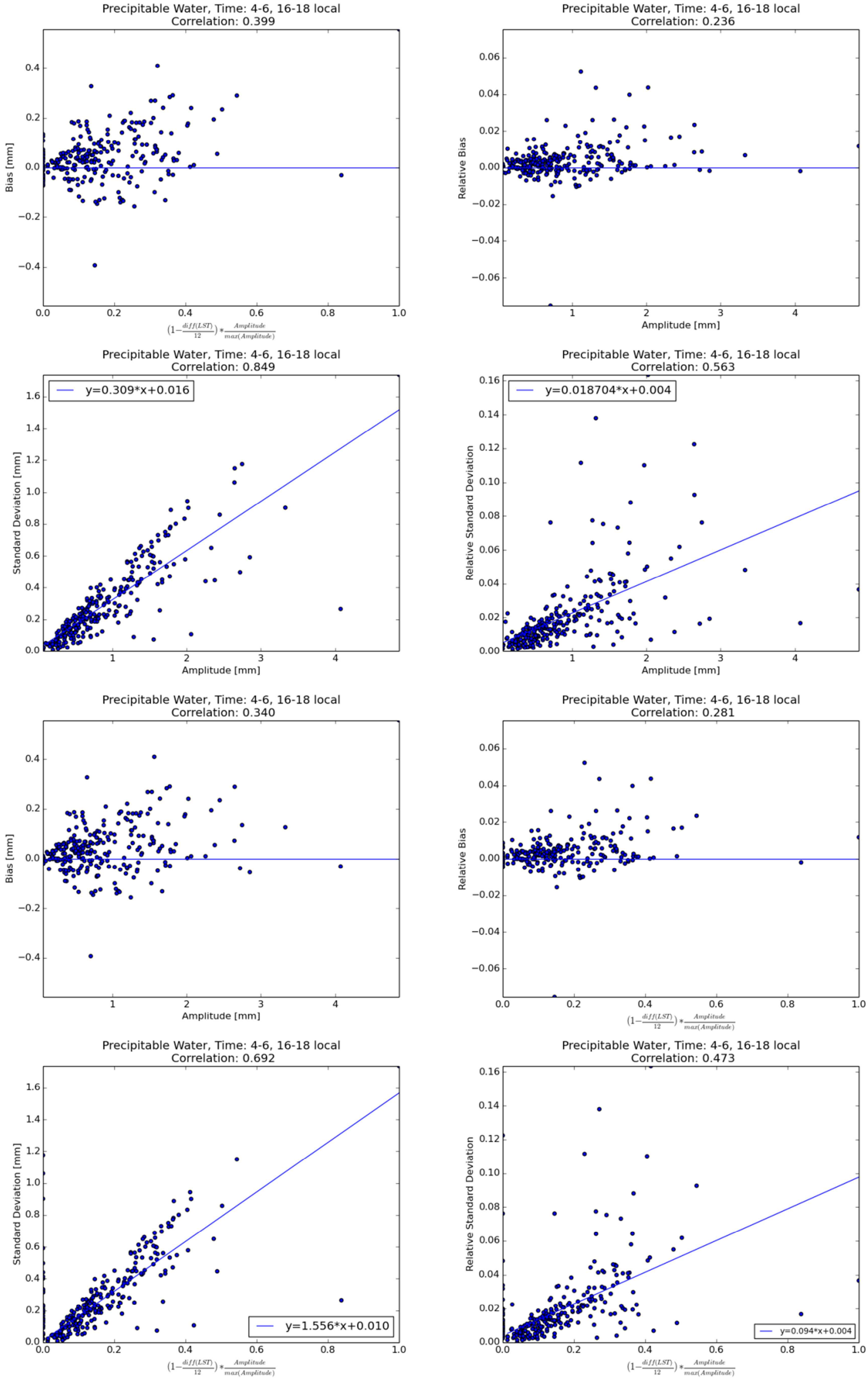

Figure 29. Several relations of absolute as well as relative bias and standard deviation. For more details, see axis labels.

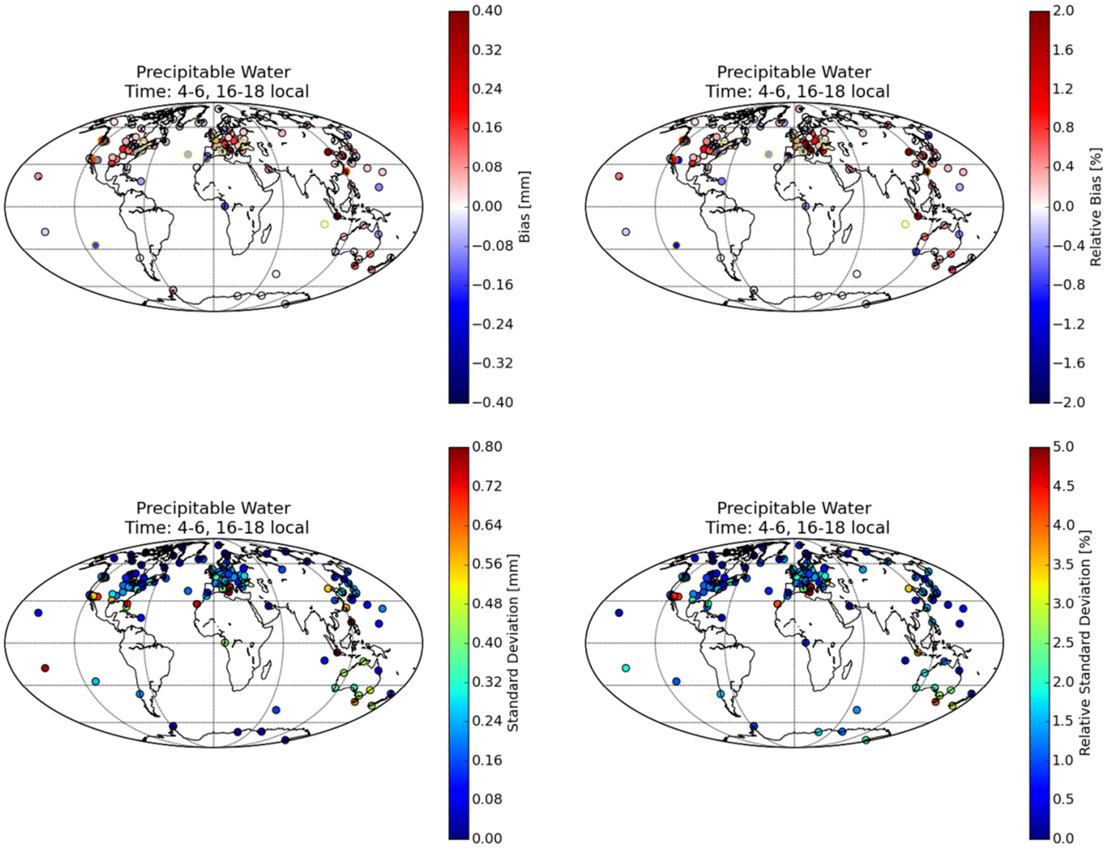

Figure 30. Differences between bias/standard deviation (left) and relative bias/standard deviation (right) for several features